2001

A programmable MEMS bandpass filter.

Sotirios. Diamantis
University of Windsor

INFORMATION TO USERS

This manuscript has been reproduced from the microfilm master. UMI films the text directly from the original or copy submitted. Thus, some thesis and dissertation copies are in typewriter face, while others may be from any type of computer printer.

The quality of this reproduction is dependent upon the quality of the copy submitted. Broken or indistinct print, colored or poor quality illustrations and photographs, print bleedthrough, substandard margins, and improper alignment can adversely affect reproduction.

In the unlikely event that the author did not send UMI a complete manuscript and there are missing pages, these will be noted. Also, if unauthorized copyright material had to be removed, a note will indicate the deletion.

Oversize materials (e.g., maps, drawings, charts) are reproduced by sectioning the original, beginning at the upper left-hand corner and continuing from left to right in equal sections with small overlaps.

Photographs included in the original manuscript have been reproduced xerographically in this copy. Higher quality 6" x 9" black and white photographic prints are available for any photographs or illustrations appearing in this copy for an additional charge. Contact UMI directly to order.

ProQuest Information and Learning
300 North Zeeb Road, Ann Arbor, MI 48106-1346 USA
800-521-0600

A PROGRAMMABLE MEMS BANDPASS FILTER

by

Sotirios Diamantis

A Thesis
Submitted to the Faculty of Graduate Studies and Research
through Electrical and Computer Engineering
in Partial Fulfillment of the Requirements for
the Degree of Master of Applied Science at the
University of Windsor

Windsor, Ontario, Canada

2000

A PROGRAMMABLE MEMS BANDPASS FILTER

by

Sotirios Diamantis

ABSTRACT

The design and simulation of a programmable microelectromechanical (MEMS) filter based on using coupled microresonators is described in this research. The filter consists of two mechanical resonators interconnected by a square-truss coupling spring. A special parallel-plate type geometry has been incorporated into the filter design to afford programmability capability.

Both lumped parameter methods based on the use of ordinary differential equations (ODEs) and finite element methods (FEA) based on the actual three-dimensional geometry have been employed in the analysis of the filter. A MEMS based filter with a programmable bandwidth of thirty percent was achieved.

To my parents

ACKNOWLEDGEMENTS

Those people who were willing to share their time and their ideas with me made this thesis possible. I first would like to express my deepest appreciation for the technical guidance and support given by my research advisor, Dr. W. C. Miller. His help coupled with an unmatchable enthusiasm for the field of MEMS will always be remembered.

I also want to express my appreciation to Dr. M. Ahmadi and Dr. G. A. Jullien for their interest in my research and their encouragement during this research project. I am grateful to Dr. W. J. Altenhof for his interest in my research and for his mechanical perspective into this project.

To Jane Black I extend my utmost thanks for helping me obtain books involving my research. The University of Windsor couldn't get a better librarian than Jane.

I want to thank Daniel Keating at IntelliSuite who provided me with truly valuable advice into the world of FEA. In addition, stimulating technical and casual conversations from Dr. Zamani, Ali Karbassian and Narinder Singh Chana.

I would also like to express my gratitude for having had the opportunity to be a member of the University of Windsor Signals and Systems Research Group.

The author whishes to acknowledge the contributions of NSERC, the INTELLISENSE corporation and the GENNUM corporation.

TABLE OF CONTENTS

LIST OF ABBREVIATIONS

AC	Alternating Current
CMOS	Complementary metal oxide semiconductor
DC	Direct Current
FEA	Finite Element Analysis
IC	Integrated Circuit
LPCVD	Low Pressure Chemical Vapor Deposition
MEMS	Micro-Electro-Mechanical Systems
PolySi	Polycrystalline Silicon
ppm/^{0}C	Percent Per Million per degree Celsius
RGT	Resonant Gate Transistor [5]
SPICE	Simulation Program with Integrated Circuit Emphasis
VCO	Voltage controlled oscillator

NOMENCLATURE

ρ	Density of PolySi
η	Theoretical transformation parameter
β	Ratio of outer to inner beam length
ω_0	Angular mechanical resonant frequency
ε_0	Permittivity of air
ω_r	Angular resonant frequency
BW_{3dB}	3-dB bandwidth
C_i	Capacitance
d	Drive/sense comb-finger spacing
D	Damping constant
d_{tri}	Tuning finger gap spacing for resonator
d_{ts}	Tuning finger gap spacing for coupling spring
E	Young's modulus
f_0	Filter center frequency
F_{e1}	Electrostatic force on first resonator
F_{e2}	Electrostatic force on second resonator
F_{ecs}	Electrostatic force on coupling spring
F_{eijy}	Electrostatic force in y direction due to tuning fingers
F_i	Filter input force
F_{iy}	Electrostatic force in y-direction due to drive fingers
h	Structural layer thickness
K_{12}	Coupling spring stiffness
K_{ei}	Electrical spring "constant"
K_i	Resonator stiffness at shuttle location
K_{mi}	Mechanical spring constant
L_{bi}	Beam length
L_i	Inductance
L_{tri}	Tuning finger overlap length for resonator
L_{ts}	Tuning finger overlap length for coupling spring
M_i	Resonator mass at shuttle location
N_i	No. of drive/sense fingers per port
N_{tri}	No. of tuning fingers per resonator
N_{ts}	No. of tuning fingers for coupling spring
Q	Quality factor
R_i	Resistance
v	Velocity
V	Voltage
V_b	Filter DC bias voltage
W_{bi}	Beam width
x	Displacement

1

INTRODUCTION

This thesis is about filters - or more precisely, programmable microelectromechanical (MEMS) bandpass filters used in signal processing applications. The term microelectromechanical comes from the transformation within this microscopic filter, of electrical signals into mechanical energy, and after the filtering takes place, the transformation of the remaining signals back into the original electrical form. The term bandpass means that the filter ideally passes all frequencies between two non-zero finite limits and attenuates frequencies not within the limits.

The use of electromechanical filters for signal processing dates back to the 1940's. In early filters, steel plates were used as resonators, and wires were used as the mechanical coupling elements [1]. Mechanical filters were refined between 1950-1970 into effective signal processing components and were designed into a variety of applications [8, 9]. They have been used where narrow bandwidth, low loss, and good stability are required. They typically have high-quality factors (Q) combined with excellent aging characteristics. In present-day mechanical filters, nickel-iron alloys are use in constructing the resonant elements, which are capable of quality factors as high as 25 000 [1].

Mechanical filters were noncompetitive because of higher manufacturing costs and larger size. The introduction of MEMS signal processing filters has eliminated many of their technological drawbacks [1], [6]. The advances in micromachining processes and in microresonator materials and design have opened the feasibility of integrated MEMS filters [2, 3]. The IC batch process is used to fabricate the resonators, coupling elements together, thereby achieving the advantages of batch fabrication and avoiding time-consuming steps such as the serial bonding of coupling wires to resonators [1]. Microresonators fabricated from polycrystalline silicon, a low-loss (high Q) material, driven by interdigitated electrodes are very attractive as building blocks for mechanical filters. Filters fabricated from LPCVD polycrystalline silicon can have low average residual strain in the film, both tensile and compressive, since they are able to release stress being freed from the substrate [1], [2].

The successful fabrication of these filters using planar integrated circuit CMOS technologies has eliminated many technological drawbacks of the past. Furthermore, their compatibility with IC processes will one day make these MEMS filters commercially available in the form of an inexpensive multifunctional chip.

1.1 ENVIRONMENTAL LIMITATIONS

Environmental limitations arising with these tiny MEMS filters are numerous. They include temperature and pressure, along with a multitude of other consequences of miniaturization that are not yet fully understood. This section suggests a hermetic sealing process [1] that solves a subset of environmental problems. Hermetic sealing refers to packaging technology designed to keep moisture from condensing inside the enclosure during exposure to the service environment.

A planar hermetic sealing process has been developed to enable high-quality factors for these MEMS filters and make possible wafer-lever vacuum encapsulations. This process uses a low-stress silicon nitride shell for vacuum sealing [1]. A wafer-level integrated vacuum-encapsulation process is especially attractive since expensive postpackaging may be avoided.

The actual layout for the vacuum-encapsulation is illustrated in Figure 1.1, where the comb-drive microstructure is covered by a microshell. The microshell is drawn transparent such that both the comb resonator and ground pane can be clearly seen.

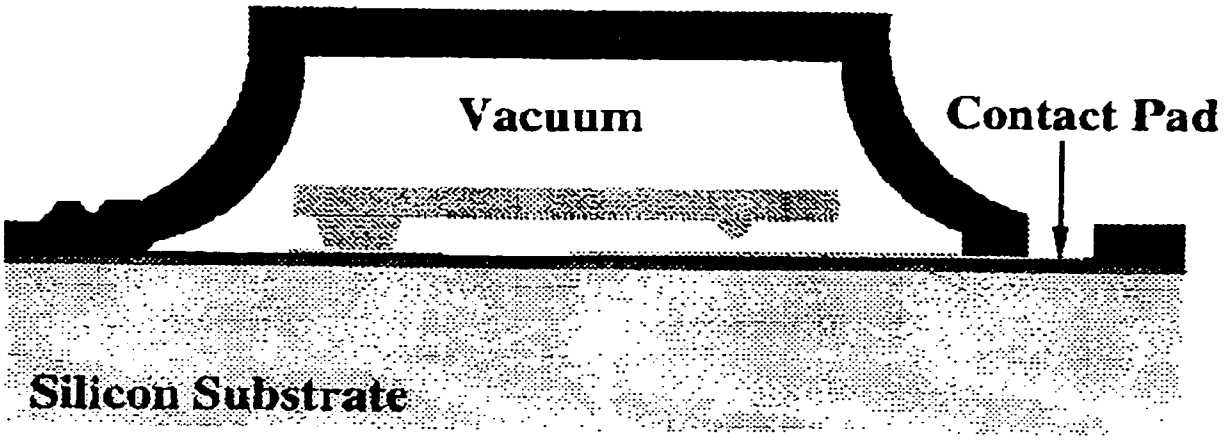

FIGURE 1.1 Vacuum encapsulated MEMS filter [1].

The process sequence begins with the standard fabrication steps described in Section 5.1. A 2-μm-thick LPCVD low-stress nitride layer is deposited at a deposition pressure of 300 mTorr to seal the shell, and contact pads are opened.

Research on the above or on other techniques for reducing the effects of the environment in microscale resonators will most likely be extremely important for improving the performance of MEMS signal processors.

1.2 THE TARGET APPLICATION

MEMS filters have been shown to be less susceptible to temperature variations than their macroscale counterparts [1, 6]. The filter characteristics are a function of Young's modulus and the density of polysilicon, both of which vary with temperature. For fine-grained polysilicon, the temperature coefficient of the resonance frequency (TC_f) can be determined by differentiating with respect to temperature T, yielding an expression of the form [1]

$$TC_f = \frac{1}{2}(TC_E + TC_h) \tag{1.1}$$

where TC_E and TC_h are the temperature coefficients of Young's modulus and thermal expansion, respectively.

In research conducted by others, [5, 6] the resulting curves are reported to show an almost linear decrease in frequency with increasing temperature. Temperature related fractional frequency variations for MEMS polycrystalline silicon filters are found in [6]. The center frequency decreases at the rate of 6.1ppm/^{0}C, and the bandwidth decreases at the rate of 564ppm/^{0}C.

The IC process is not sufficiently controlled so that the microresonators can be fabricated without some means of trimming for final adjustment of the filter characteristics. The average resonance frequency mismatch in present day fabrication processes is 0.4-0.7% [6, 9]. This degree of mismatch is sufficient to cause significant passband distortion in the filter. In order to trim the resonant frequencies, processes for adding or removing material from the resonator must be utilized [1].

Recent developments in "electrical trimming" by using parallel-plate structures to exert electrostatic forces seems to provide a way for postprocess trimming [6]. If successfully developed, this method can potentially solve the

controllable and repeatable problems for these MEMS filters as well as providing a programmable filter capability [1].

1.3 A PREVIOUS ATTEMPT AT CONTROLLABILITY

The MEMS filter, depicted in Figure 1.2 [6], was one of the very first attempts at tuning the individual resonators center frequencies using parallel plate capacitor transducers. These resonators were fabricated by Wang and coworkers at the University of Michigan. The device shown in Figure 1.2 consisted of three tunable microresonators coupled by springs. Frequency-tunable resonators were used to alleviate nonideal effects and are key to successful microscale mechanical filter implementation.

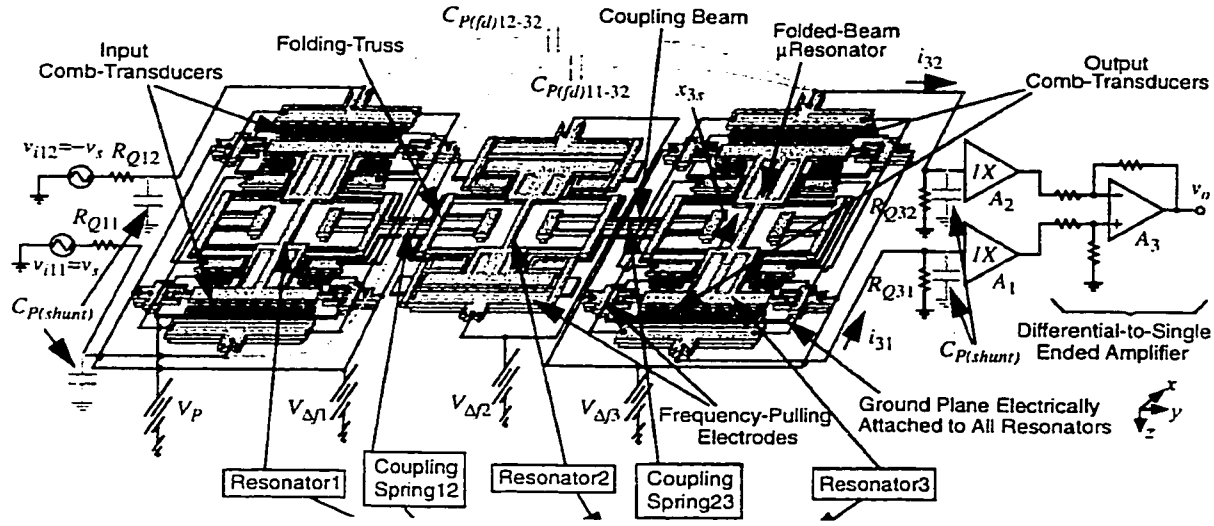

FIGURE 1.2 Schematic of a three-resonator, micromechanical filter. The parallel-plate capacitive transducers that allow voltage controlled tuning of individual resonator center frequencies [6].

1.3 OVERVIEW

This thesis will focus upon controlling the spectral properties of a programmable MEMS bandpass filter. Chapter 2 presents an in depth discussion of programmable MEMS filters, from their basic operation, to circuit modeling, to the electrical spring constant. In Chapter 3, the complete design procedure is described and then used in the context of an example. For this purpose, the 21 KHz, 1.1 kHz bandwidth, two-resonator programmable MEMS filter demonstrated in this work will be used. Chapter 4 discusses the dynamic system modeling using SIMULINK. The system is modeled in SIMULINK using ordinary differential equations (ODEs). The effectiveness of masked subsystem models and S-Functions that make it easier to model and visualize the process are carefully examined. Chapter 5 begins by addressing the fabrication of MEMS filters. This fabrication technique involves a sequence of depositions and patternings to achieve a structure in which the film-to-be-suspended sits upon a sacrificial film, which is exposed to the surface and can be accessed by etchants. A sacrificial etch then removes the sacrificial layer, freeing the structure in the process. The programmable frequency ranges of both the individual resonators and the two-resonator filter will be demonstrated by a 3-D FEA simulation with IntelliSuite software. A comparison of values computed using lumped parameter methods (ODEs) and distributed parameter methods (3-D FEA) will be carried out.

2

MEMS FILTER OPERATION

Every mechanical structure has an infinite number of resonance frequencies. The two-resonator MEMS filter has two natural resonances of interest. The relative spacing between these two mode peaks determines the passband of the eventual filter. Emphasizing a particular resonance frequency is generally approached through considerations of resonator geometry and the properties of its structural material. Since planar and bulk micromachining fabrication technologies can realize a large variety of geometries, usually in only few masking steps, these technologies provide substantial design flexibility for resonators [14]. A wide variety of publications are available which describe different resonator geometries and materials, both macroscopic and microscopic.

This chapter begins with an in depth discussion on the operation of a programmable two-resonator MEMS filter. Analysis will be performed in terms of its geometric design, which determines the frequency spectrum of the filter. Equivalent circuits models are developed that allow us to apply a large body of mechanical and electrical filter design tools. Finally, the theory behind the "electro-spring" (due to the parallel-plate capacitor structures) is presented.

2.1 MEMS FILTER OVERVIEW

Figure 2.1 presents the proposed overhead-view schematic for the programmable two-resonator MEMS filter of this work, to be described in great detail in subsequent sections. Spring K_{12} links two adjacent resonators having masses M_1 and M_2 and springs K_1 and K_2.

This MEMS filter features parallel-plate capacitive structures that allow for the voltage controlled tuning of the filter spectral properties. Parallel-plate structures have been used extensively in the past in a variety of different geometries and structures. Their particular placement on this structure may offer remarkable results in frequency programmability.

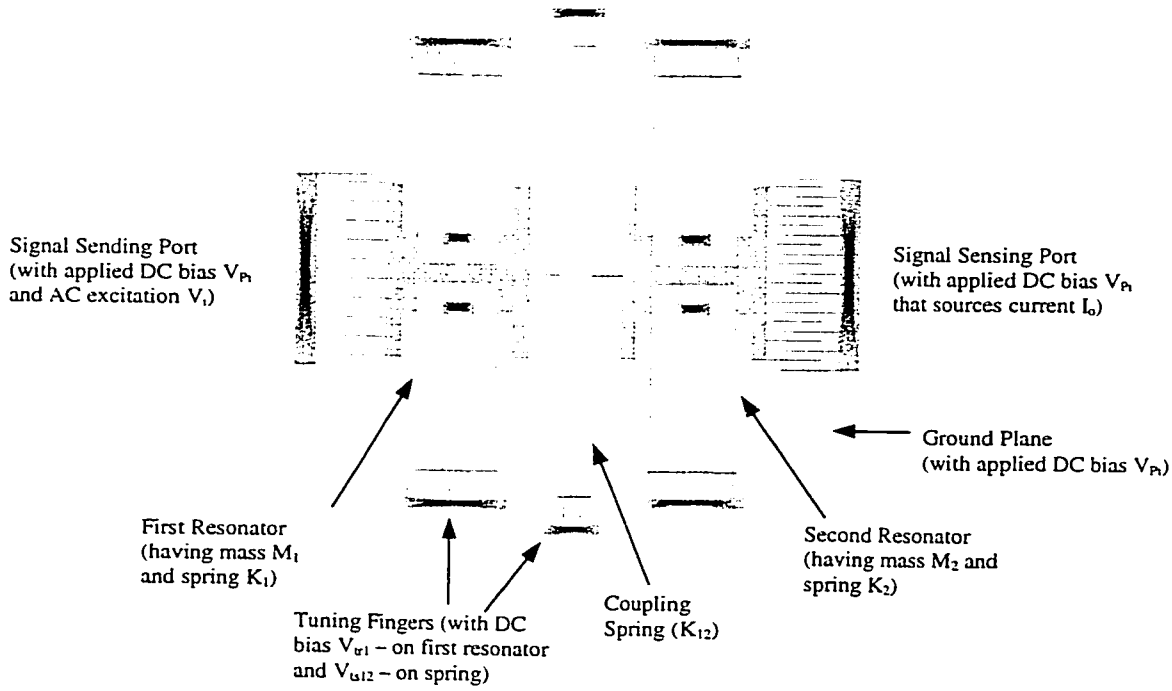

FIGURE 2.1 Two-resonator programmable MEMS filter.

Comb drive micro-mechanical-structures, shown in Figure 2.1, are the most frequently encountered type of MEMS devices. Figure 2.2 is a close-up view of the comb-drive structure. Since comb drive structures can have many "fingers", for simplicity, Figure 2.2 shows only a portion of the structure. There are two types of fields generated by the potential difference between the fixed and movable fingers; they are the local and global electric fields.

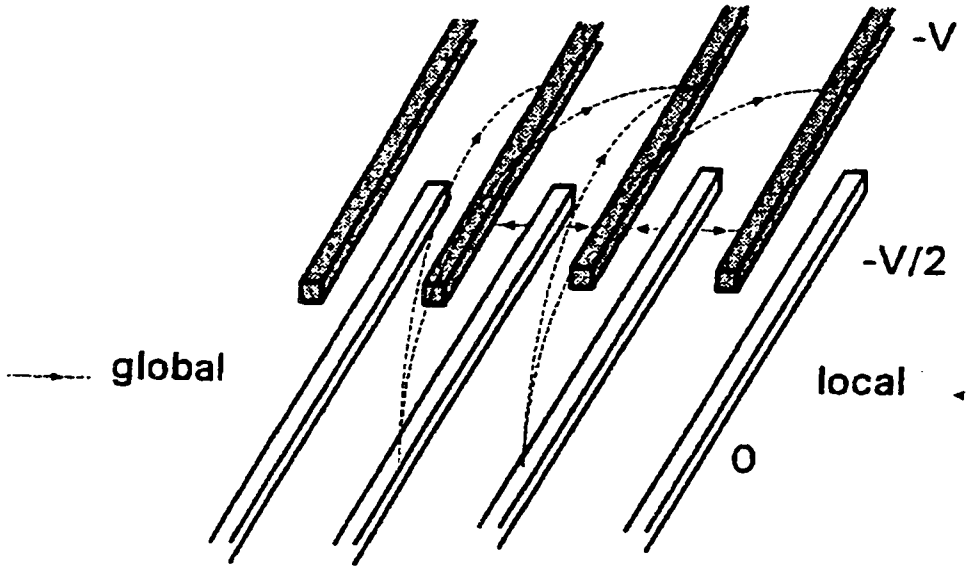

FIGURE 2.2 The geometry of a micromechanical comb drive actuator with local and global electric fields. Since there are typically a large number of fingers, only four fixed (at potential -V) and four movable (at potential 0) fingers are shown [16].

Global forces create an attractive force between two long parallel filaments of electric current, yielding the attractive force (per unit length) for these free-space magnetic line currents. This attractive electrical force pulls the line currents together and thus acts in the direction parallel to the fingers [16]. These forces are what allow us to drive the filter into lateral-directed motion at the frequency of voltage V_i applied to the signal sending port (Figure 2.1).

Local fields remain confined to the finger cross-sections (movable plus fixed finger cross-section region) [16]. A two-dimensional cross-section analysis is presented in Section 2.3 as the static capacitance between the movable and fixed electrode give rise to an electrostatic spring constant that allows frequency programmability.

Each resonator consists of a movable shuttle suspended a few microns (2 μm for this work) above the substrate by the beam flexures. The flexures are anchored near the center of the structure to an underlying ground plane. The ground plane is necessary; if it is not present, the resonator may pull-in to the substrate with even small (0.5V) voltage differences [14].

As shown in Figure 2.1, under normal operation a DC bias voltage (V_{Pi}) is applied to the conductive filter structure, while an AC excitation voltage (V_i) is applied to the signal sending port. This voltage combination generates a force component proportional to the product $V_{Pi}V_i$ that drives the mechanical system into lateral-directed resonance when the frequency of V_i falls within the filter passband. Motion of the output resonator then creates a DC biased time-varying capacitor at the output port $C_o(t)$, that in turn sources an output current given by [14]

$$i_0 = V_{Pi}\frac{\partial C_0}{\partial t} \tag{2.1}$$

In effect, the electrical input signals are converted to mechanical signals, processed in the mechanical domain and re-converted to electrical signals at the output.

2.2 THEORETICAL MODELING

2.2.1 Mechanical Model

As a starting point in dealing with this spring-mass system we will first consider the components themselves. We assume that the springs are massless and are linear, that is, they obeys Hook's law (Force is proportional to displacement). The resonator mass elements are assumed to be rigid and concentrated at a single point, the shuttle (body of the resonator). Our final assumption is that the vibration amplitude is small and therefore the masses move laterally along a straight line (one-dimensional problem). The resonant frequency of this resonator is given by

$$f_i = \frac{1}{2\pi}\sqrt{\frac{K_i}{M_i}} \tag{2.2}$$

where M_i and K_i is the mass and spring coefficient of the i^{th} resonator. The derivation of the effective mass and stiffness of a MEMS resonator is presented in Appendix A. The effective mass at the shuttle given for the general case is

$$M_i = M_s + \frac{M_t}{(1+\beta^3)^2} + \frac{13}{35(1+\beta^3)^2}M_{bi} + \left[\frac{1}{(1+\beta^3)} + \frac{13\beta^6}{35(1+\beta^3)^2}\right]M_{bo} \tag{2.3}$$

where subscripts s, bi, bo and t correspond to the shuttle, the inner and outer beams, and the trusses, respectively. β represents the ratio of the outer beam length L_{bo} to the inner beam length L_{bi}. The stiffness at the shuttle location is

$$K_i = \frac{4Eh}{1+\beta^3}\left(\frac{W}{L_{bi}}\right)^3 \tag{2.4}$$

where W is the width of the eight beams. The thickness of the microstructure is h, and Young's modulus of polysilicon is E.

The spectrum in the frequency domain is determined by the filter's modes of vibration that are a function of the individual resonators oscillation frequencies and coupling spring stiffness as well as the coupling spring's finite mass. These values of equivalent mass and springs can be designed by changing the filter geometry.

The mechanical model of the MEMS filter from Figure 2.1 has been developed and is present in Figure 2.6. This mechanical model was developed using free-body-diagrams for each mass M_1, M_2 and M_3 as presented in Figures 2.3, 2.4, and 2.5 respectively.

The forces acting on M_1 (as illustrated in Figure 2.3) are due to:

1) The longitudinal force (F_i) and the transverse force (F_{iy}) developed by the drive electrodes.
2) The longitudinal force (F_{e1}) and transverse force (F_{e1y}) developed by the tuning electrodes.
3) The force transmitted through the spring connecting M_1 and M_3, and finally,
4) The forces due to the resonator spring constant K_1 and damping coefficient D_1.

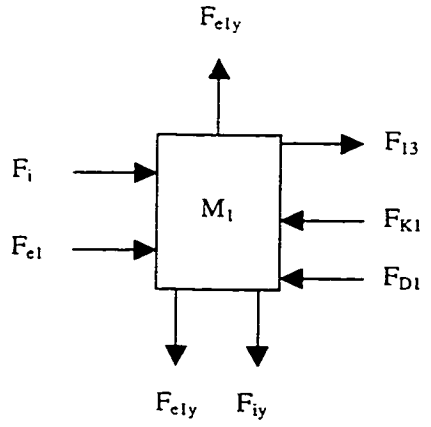

FIGURE 2.3 The total forces acting on M_1.

The forces acting on M_2 (as illustrated in Figure 2.4) are due to:

1) The longitudinal force (F_{e2}) and transverse force (F_{e2y}) developed by the tuning electrodes.
2) The force transmitted through the spring connecting M_3 and M_2, and finally,
3) The forces due to the resonator spring constant K_2 and damping coefficient D_2.

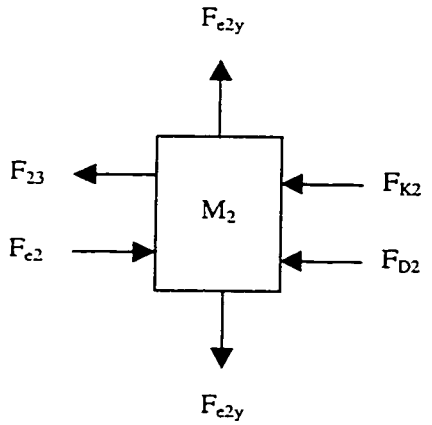

FIGURE 2.4 The total forces acting on M_2.

The forces acting on M_3 (as illustrated in Figure 2.5) are due to:

1) The longitudinal force (F_{ecs}) and transverse force (F_{escy}) developed by the tuning electrodes.
2) The force transmitted through the spring connecting M_1 and M_3 and the spring connecting M_2 and M_3.

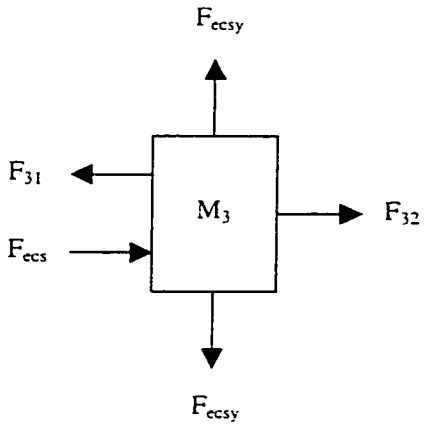

FIGURE 2.5 The total forces acting on M_3.

Forces F_{e1}, F_{e2} and F_{ecs} are the electrostatic forces generated by the parallel plate structures applied to resonator one, two, and the coupling spring, respectively. Note that these forces are distributed at the top and bottom of the structure, however for our purposes are lumped into one force. Forces F_{e1y}, F_{e2y}, and F_{ecsy} are the y-component of force generated by the parallel plate tuning structures; these forces cancel each other. Force F_{iy} is the y-component of force generated by the drive electrodes that is assumed to be negligible, thus all forces acting on each mass is in the longitudinal direction, simplifying this to motion in only one direction.

The equations of motion can be developed from these free-body-diagrams. Spring K_{12}, having a finite mass M_3, links two adjacent resonators having masses M_1 and M_2, spring constants K_1 and K_2 and damping coefficients D_1 and D_2, respectively. The system has three degrees of freedom, X_1, X_2 and X_3, thus three simultaneous equations are required to describe the system. The three equations come from the free-body diagrams of each mass. Other analyses assume only two masses, however, we have utilized a third mass (termed M_3) to accurately analyze the electrostatic forces on the coupling spring.

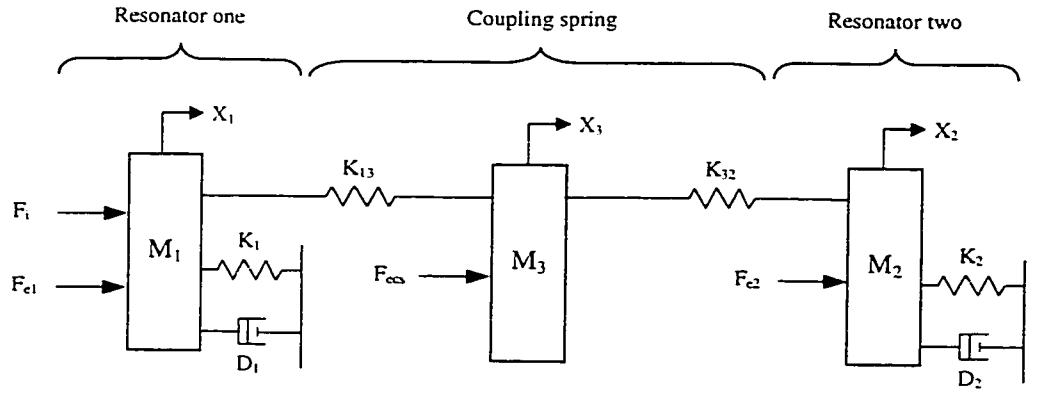

FIGURE 2.6 Mechanical model of programmable two-resonator MEMS filter.

The equations of motion can now be written for resonator one as:

$$\sum \vec{F}_1 = M_1 \ddot{\vec{X}}_1$$

$$\vec{F}_i + \vec{F}_{e1} - K_1 \vec{X}_1 - D_1 \dot{\vec{X}}_1 + K_{13}\left(\vec{X}_3 - \vec{X}_1\right) = M_1 \ddot{\vec{X}}_1 \tag{2.5}$$

and for the coupling spring

$$\sum \vec{F}_3 = M_3 \ddot{\vec{X}}_3$$

$$K_{13}\left(\vec{X}_1 - \vec{X}_3\right) + \vec{F}_{ecs} + K_{32}\left(\vec{X}_2 - \vec{X}_3\right) = M_3 \ddot{\vec{X}}_3 \tag{2.6}$$

and for the second resonator

$$\sum \vec{F}_2 = M_2 \ddot{\vec{X}}_2$$

$$\vec{F}_{e2} - K_2 \vec{X}_2 - D_2 \dot{\vec{X}}_2 + K_{32}\left(\vec{X}_3 - \vec{X}_2\right) = M_2 \ddot{\vec{X}}_2 \tag{2.7}$$

In the next section we will see that these electrostatic forces give rise to an electrostatic spring constant, termed electro-spring. Sufficing to say for now that $\mathbf{F}_{e1}=K_{e1}\mathbf{X}_1$, $\mathbf{F}_{e2}=K_{e2}\mathbf{X}_2$ and $\mathbf{F}_{ecs}=K_{ecs}\mathbf{X}_3$. Where K_{e1}, K_{e2} and K_{ecs} are the electrostatic springs relating applied force to displacement for the first resonator, second resonator and coupling spring, respectively.

Utilizing the Laplace transform and Cramer's rule we can develop a relation between the output displacement ($\mathbf{X}_2$) and the input force ($\mathbf{F}_i$). The transfer function of the output displacement to the input force is essential since the derivative of the output displacement is proportional to the sense current and the drive force to the applied input voltage.

$$\frac{X_2}{F_i}=\frac{K_{13}(-K_{32}-K_{ecs})}{\begin{vmatrix} M_1S^2+D_1S+K_1+K_{13}-K_{e1} & 0 & -K_{13} \\ -K_{13} & -K_{32}-K_{e2} & M_3S^2+K_{32}+K_{13} \\ 0 & M_2S^2+D_2S+K_2+K_{32} & -K_{32}-K_{ecs} \end{vmatrix}} \tag{2.8}$$

2.2.2 Electrical Model

Mechanical systems parallel electrical networks to such an extent that there are analogies between electrical and mechanical components and variables. Mechanical systems, like electrical networks, have three passive, linear components. Two of them, the spring and the mass, are energy-storage elements; one of them the viscous damper, dissipates energy. The two energy storage elements are analogous to the two electrical energy-storage elements, the inductor and capacitor. The energy dissipater is analogous to electrical resistance. Moreover, mechanical force is analogous to electrical voltage and mechanical velocity is analogous to electrical current which leads to the analogy

between the mechanical displacement and electrical charge. A network of lumped elements can describe both electrical and mechanical circuits. Both circuits have poles and zeros and can be described by mathematical function that approximate the filter's actual frequency response. Table 2.1 is a summary of the above analogies.

Mechanical Variable	Electrical Variable
Damping, D	Resistance, R
Stiffness^{-1}, K^{-1}	Capacitance, C
Mass, M	Inductance, L
Force, F	Voltage, V
Velocity, v	Current, I

TABLE 2.1 Mechanical-Electrical analogies.

From an electronic system design standpoint, the transfer function relating input voltage to output current I_o/V_i is most useful. Such a relation may be obtained by relating the internal mechanical parameters F_i and X_2 to the corresponding electrical input and output through the phasor relations described in [1]. Hence, the filter transconductance can be expressed in phasor form as

$$\frac{I_o}{V_i} = SV_{Pi}^2\left(\frac{\partial C}{\partial x}\right)_i\left(\frac{\partial C}{\partial x}\right)_o \cdot \left(\frac{X_2}{F_i}\right) \tag{2.9}$$

The nominal response of the mechanical equivalent circuit for the two-resonator filter can be further illustrated for a purely electrical model. The electrical elements for inductance L_i, capacitance C_i and resistance R_i are related to the mechanical elements mass M_i, stiffness K_i and damping D_i as follows [1]

$$L_i = M_i\eta^2 \tag{2.10}$$

$$C_i = \frac{1}{K_i\eta^2} \tag{2.11}$$

$$R_i = D_i\eta^2 \tag{2.12}$$

$$C_{ij} = \frac{1}{K_{ij}\eta^2} \tag{2.13}$$

where the theoretical transformation parameter having units (Volts Farads / meter)$^{-1}$ is defined as [1]

$$\eta = \frac{1}{V_{Pi}\left(\frac{\partial C}{\partial x}\right)_i} \tag{2.14}$$

For the particular case of comb-driven transducers, the value of $\partial C/\partial x$ is a constant and can be theoretically approximated at the drive and sense ports as [1]

$$\frac{\partial C}{\partial x} = \frac{2N\varepsilon_0 h}{d} \tag{2.15}$$

where N is the number of comb fingers, ε_0 is the permittivity constant, d is the gap between the fingers and h is the structural thickness.

The electrical equivalent circuit for the two-resonator MEMS filter is shown in Figure 2.7. A large body of electrical filter design tools can now be applied.

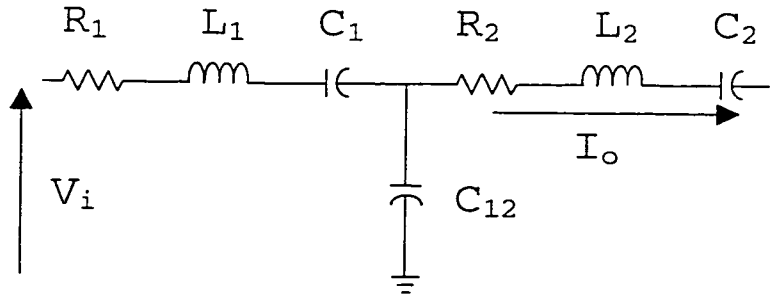

FIGURE 2.7 Equivalent circuit for the two-resonator MEMS filter.

2.3 THEORY OF THE PROGRAMMABLE STRUCTURE

Programmability for our purposes refers to the variability of the center frequency as well as that of the bandwidth for the two-resonator MEMS bandpass filter. As previously mentioned, this spring constant is relatively useful in voltage controlled oscillator (VCO) applications of mechanical structures. The history of experimentation with the electrical spring constant goes as far back as 1967, conducted by Nathanson and coworkers from Westinghouse in their resonant gate transistor (RGT) project [5].

Despite all the research conducted in this area, it is still not certain how much programmability the two-resonator MEMS bandpass filter can attain. The most recent application of the electrical spring constant has been the tuning of individual resonator's center frequency, which is discussed in Section 1.3.

The electrical spring constant generated by the parallel-plate structures on the two-resonator MEMS filter, shown in Figure 2.1, subtract from the mechanical stiffness of the filter, as will be shown below. This in turn changes the filter's frequency characteristics since frequency is dependent on the stiffness.

Both resonators and coupling spring are each equipped with parallel-plate capacitor structures that allow for voltage controlled frequency tuning via inherent electrostatic spring constants. This section presents the theory behind the electrical spring constants and how they affect each of the two vibrational modes of this programmable two-resonator MEMS filter. Figure 2.8 shows the geometry of the parallel-plate capacitor structures that are placed on the top and bottom of the programmable filter in Figure 2.1.

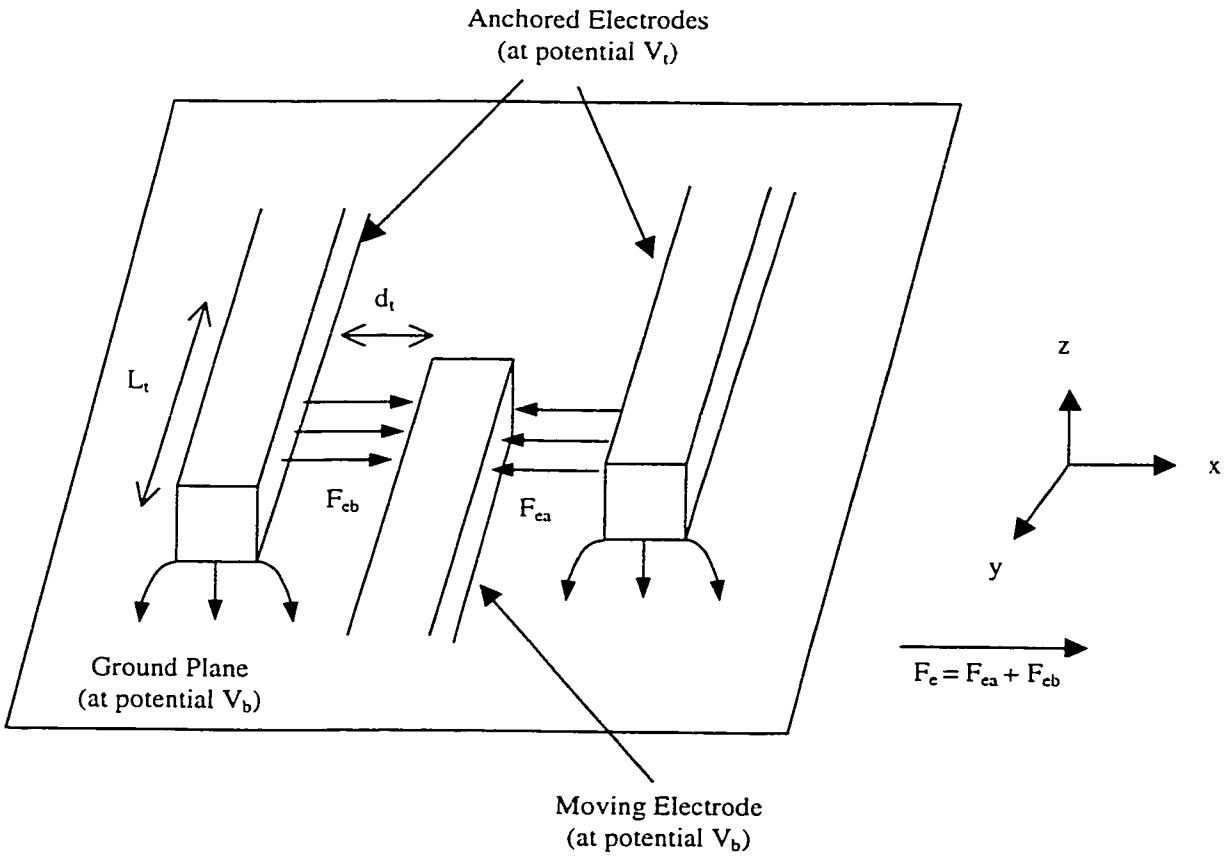

FIGURE 2.8 Three-dimensional view of the parallel-plate capacitor structures that give rise to the electro-spring and allow for voltage controlled frequency programmability.

The electrode-to-resonator capacitance C(x) is a nonlinear function of displacement (x) [14]

$$C(x) = \frac{\varepsilon_0 A_o}{d_t + x} = C_o\left(1 + \frac{x}{d_t}\right)^{-1} \tag{2.16}$$

where Ao is the beam to tune electrode overlap area, and Co is the static capacitance between the tune electrode and beam. Differentiating Equation 2.16 we obtain

$$\frac{\partial C}{\partial x} = -\frac{C_o}{d_t}\left(1 + \frac{x}{d_t}\right)^{-2} \tag{2.17}$$

where the corresponding $\partial C/\partial x$ is a function of x.

Consequently, the filter drive force F_x is dependent on not only the drive voltage V_i, but also the tuning finger force F_e. This latter dependence leads to an effective electrostatic spring constant [6, 14] that adds to the mechanical spring constant, and thus, pulls the frequencies of the MEMS filter.

To show this explicitly, we refer to Figure 2.8, and assume for the moment that there is only one fixed tuning electrode: the one on the left. The expression for the change in capacitance per unit displacement at this electrode is given by equation 2.18. Note that the direction for positive displacements is given in Figure 2.8. A Taylor series expansion may be performed on Equation 2.17.

$$\frac{\partial C}{\partial x} = -\frac{C_o}{d_t}\left(1 - \frac{2}{d_t}x + \frac{3}{d_t^2}x^2 - \frac{4}{d_t^3}x^3 + \ldots\right) \tag{2.18}$$

assuming small displacements we retain only the first two terms of Equation 2.18 [6, 14]. The drive force due to the electrostatic force can now be written as [14]

$$F_{ea} = \frac{1}{2}(V_b - V_t)^2 \frac{\partial C}{\partial x} \approx \frac{1}{2}(V_b - V_t)^2\left[-\frac{C_o}{d_t} + \frac{2C_0}{d_t^2}x\right] \tag{2.19}$$

The first term in Equation 2.19 represents a drive force arising from the left fixed electrode's electrostatic voltage (V_b-V_t). This force is not dependent on displacement x. The second term represents an additional force component that has a displacement dependence. This electrostatic force component is similar to the mechanical spring restoring force of the resonator. However, while the mechanical spring restoring force generally acts to oppose an input force, this force acts to increase the input force. This second term, in fact, can be interpreted as an electrical spring constant [6, 14]

$$K_{ea} = (V_b - V_t)^2 \frac{C_0}{d_t^2} \tag{2.20}$$

which subtracts from the mechanical spring constant, changing the resonance frequency. Note the dimensions of the electrostatic spring (N/m) as

$$\frac{V^2F}{m^2} = \frac{(N \cdot m/C)^2 (C^2/N \cdot m)}{m^2} = \frac{N}{m} \tag{2.21}$$

The fixed electrode on the right hand side will also contribute an electrical spring constant that must be added to the expression in Equation 2.20. Applying an analysis similar to the above, the force due to port 2 is given by [6, 14]

$$F_{eb} = \frac{1}{2}(V_b - V_t)^2 \left[\frac{C_o}{d_t} + \frac{2C_0}{d_t^2}x\right] \tag{2.22}$$

where the total force acting on the moving electrode is $F_e = F_{ea} + F_{eb}$ and the total electrical spring constant becomes [6, 14]

$$K_e = 2(V_b - V_t)^2 \frac{C_0}{d_t^2} \tag{2.23}$$

In Equation 2.23, C_o is the tuning electrode-to-resonator overlap capacitance given by [6]

$$C_o = \frac{2\xi_t N_t \varepsilon_0 h L_0}{d_t} \tag{2.24}$$

where N_t is the total number of tuning electrodes, ξ_t is a fringing field factor for the tuning finger overlap capacitance, and d_t and L_t are the tuning electrode-to-resonator gap spacing and overlap length, respectively. Note that the presence of gaps on both sides of the shuttle tuning fingers does not alter their function; i.e., electrical stiffness does not cancel in symmetric configurations [6, 14]. The maximum applied force on the moving electrode $F_{e(max)}$, assuming a maximum resonator displacement of 0.1μm, a structural thickness h=2μm, an electrode overlap length L_t=10μm and an electrode separation d_t=2μm is shown in Figure 2.9.

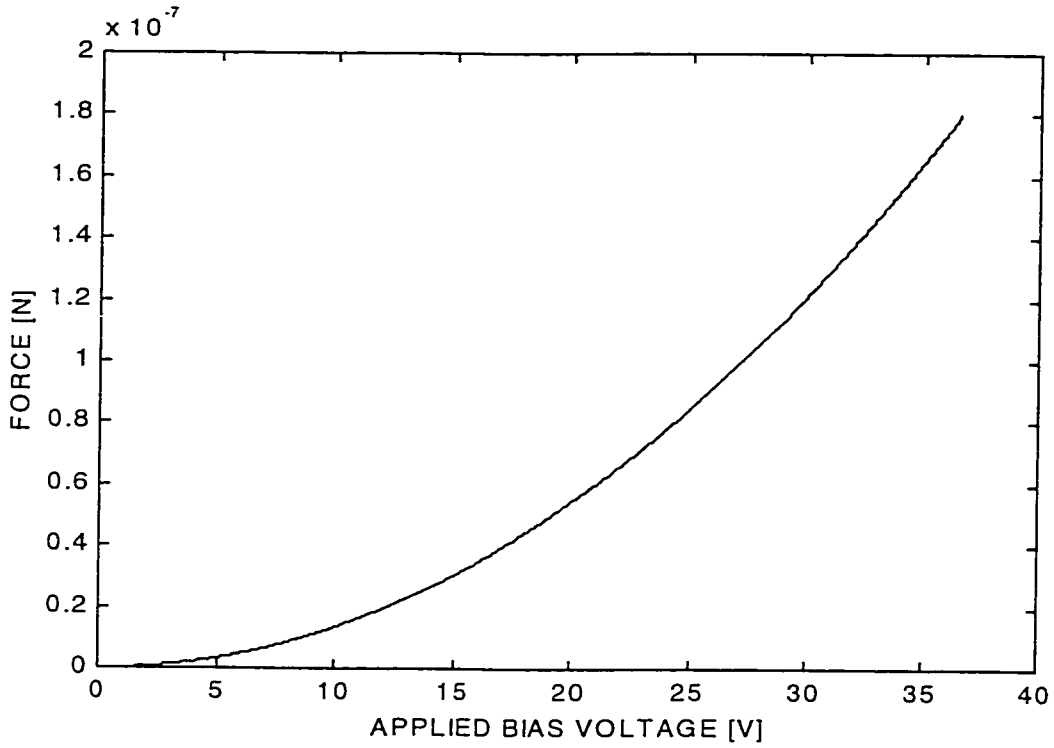

FIGURE 2.9 Electrostatic x-directed force generated by parallel-plate structures onto moving electrode versus applied bias voltage.

The dependence of frequency on tuning voltage for resonator i then follows from Equations 2.23 and 2.24, and is given by [6, 14]

$$f_r = \frac{1}{2\pi}\sqrt{\frac{K_i - K_{ei}}{M_i}} \tag{2.25}$$

where K_i is the nominal mechanical stiffness at the shuttle location (with $K_{ei}=0$).

In Equation 2.25 we assumed that the tuning fingers are placed on the resonator shuttle. If however the tuning fingers are placed on the trusses then the effective electrical stiffness seen by the shuttle has to be found. The trusses are moving at half the velocity of their shuttle masses [27]. Given that the magnitude of the shuttle mass velocity is $V_0 = \omega_0 X_0$, yields [27]

$$K_{truss} = 4K_{shuttle} \tag{2.26}$$

where $K_{shuttle}$ is the effective spring stiffness seen at the shuttle location. This means than the electrical stiffness is four times less if tuning occurs at the truss rather than at the shuttle. The advantages of tuning at the truss location is that the undesired effects of the approximation of Equation 2.19 can be further reduced for the same displacement of the resonator shuttle and the same tuning finger gap. Also, if the tuning fingers are on the truss, a greater number of them can be added to each resonator, thus reducing the amount of voltage (200 Volts) reported in [6].

The relationships between the effects of the spring constant on the single resonator's vibrational frequency, are fairly easily obtained. However, such is not the case in the two-resonator filter, whose relationships are difficult to obtain, unless conducting FEA such as employed in Chapter 5. It is possible to have some idea of the results, simply by examining the equations (for the two modes of vibration we are interest in) being used in the filter design process. This area will be discussed in Chapter 3.

It can be incurred that the square of the voltage difference between the fixed and moving electrodes will cause the electric spring constant to decrease in value quite rapidly as voltage increases. It is for this reason that the programmability ranges may not be as large as predicted by the theoretical equations. FEA simulations may be able to predict a realistic range.

2.4 DISCUSSION

Chapter 2 begins with a proposed geometry for a programmable two-resonator MEMS filter. This MEMS filter features parallel-plate capacitive structures that allow for voltage-controlled variations of its center frequency and

bandwidth. The theoretical modeling for this programmable filter is examined with the use of a mechanical lumped parameter model. Using electro-mechanical analogies this mechanical model is converted to an equivalent electrical network. The theory of the programmable structure is examined and the pertinent equations relating electrostatic force to displacement giving rise to the electro-spring (an inherent electrostatic spring) are presented.

3

MEMS FILTER DESIGN

In the previous chapter the proposed design of the two-resonator MEMS filter was discussed. This distributed mechanical network was converted to a mechanical lumped-element circuit composed of springs, masses and dampers. The mechanical circuit was then converted to its electrical analogy. This equivalence is most helpful in understanding and analyzing the characteristics of the entire filter since most computer programs and literature for filter design are expressed in electrical terms. The fact that the electromechanical filter can be converted, on paper, to an "all-electrical" network is very important since one can use SPICE to analyze its frequency response.

The programmable structures that allow voltage-controlled variations in frequency via inherent electrostatic spring constants were presented in Section 2.3. Chapter 3 will examine the MEMS filter design, using electrical analogies and SPICE, as well as expand on the electrical spring constant and how it affects the two vibrational modes of the two-resonator MEMS filter.

Figure 3.1 presents an ideal bandpass filter spectrum and defines parameters typically used for filter specification. The curve corresponds to the current expressed in decibels (dB) at the signal sensing port (Figure 2.1). The

input signal is a constant voltage, variable frequency sinusoidal wave. The transmission of the input voltage is measured with respect to the maximum voltage output. The difference between the two frequencies corresponding to the 3-dB point is the 3-dB bandwidth, BW_{3dB}. The region between the two 3-dB frequencies is the filter passband, while the frequencies outside the 40-dB points is the filter stopband. The center frequency f_0 is defined as the frequency midway between the 3-dB frequencies.

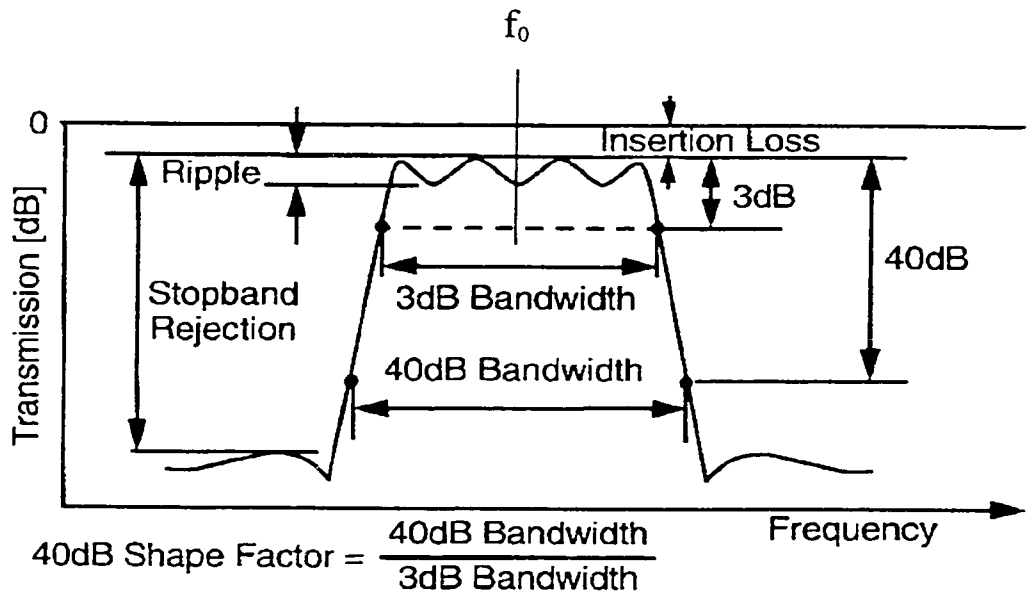

FIGURE 3.1 Parameters typically used for filter specification [6].

Having defined the frequency characteristics for the MEMS filter, we will now look at the elements, which when properly combined achieve a desired response. Although the interactions between the resonators and coupling elements are quite complex, their functions as lumped elements are roughly as follows [4]: The filter's position in the frequency spectrum is defined by the center frequency, which is determined by the individual resonators vibrational frequencies. The filter bandwidth is a function of the equivalent mass and

compliance of the resonators and the compliance of the coupling spring. The bandwidth increase as either the equivalent mass or the compliance decreases.

The details for each step of the design procedure are described in the context of an example. For this purpose the 21 kHz, 1.1 kHz bandwidth, programmable two-resonator MEMS filter developed in this chapter will be used. The design begins with specifications of the resonators with resonant frequencies near f_0 and with reasonable stiffnesses K_i. The coupling spring is chosen with an appropriate K_{12} value to achieve a desired bandwidth. The elements in the mechanical lumped equivalent model are then matched to a lumped electrical equivalent model via electromechanical analogy, where inductance, capacitance, and resistance in the electrical domain equate to mass, compliance, and damping, respectively, in the mechanical domain. These lumped parameter models (ODEs) predicted here in SPICE will be compared to the 3-D FEA simulation results with IntelliSuite in Section 5.2.

3.1 GENERAL MEMS FILTER DESIGN CONCEPTS

Figure 3.2 illustrates the principle of the two-resonator MEMS filter. Spring K_{12} links two adjacent resonators having masses M_1 and M_2 and spring K_1 and K_2.

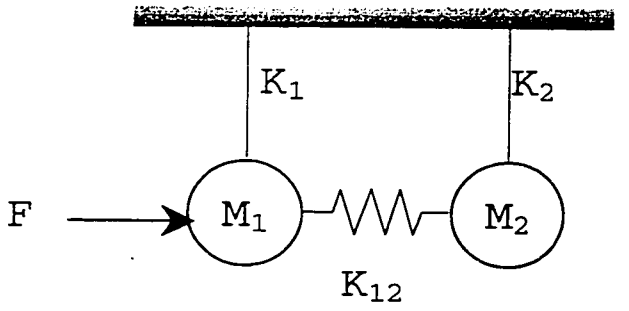

FIGURE 3.2 Conceptual diagram of a two-resonator MEMS filter.

For the moment we assume that there are no other forces applied to the filter other than the drive force shown in Figure 3.2. The electrostatic forces that give rise to inherent electrical spring constants will be discussed in subsequent sections. These forces will affect the natural modes of vibration of the filter and will be given special consideration.

In practical implementations, because planar IC processes typical exhibit substantially better matching tolerances than absolute, the constituent resonators in MEMS filter are preferably designed to be identical, with identical spring dimensions and resonance frequencies [6] with $M_1=M_2$ and $K_1=K_2$. The motion of the 1st resonator is shown in exaggerated form in Figure 3.3.

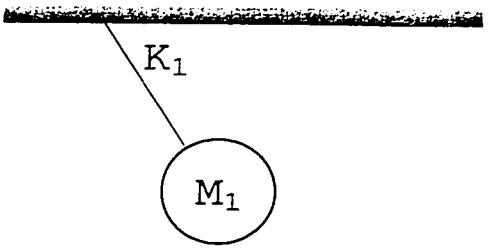

FIGURE 3.3 Single-resonator natural mode of vibration.

Since we are assuming small displacements, we can neglect the rotation of the mass and other second-order effects [4]. The resonance frequency of this simple spring and mass is

$$f_1 = \frac{1}{2\pi}\sqrt{\frac{K_1}{M_1}} \tag{3.1}$$

If we then consider the two resonators are tuned to the same frequency f_i are located side-by-side, and vibrate as shown in Figure 3.4, we can see the spring K_{12} can be removed without affecting the vibration of the system [4]. In other words, if we displace the two masses an equal distance in the same

direction and let go, there will be no forces applied to spring K_{12} and the resonators will vibrate at frequency f_1 and only at frequency f_1.

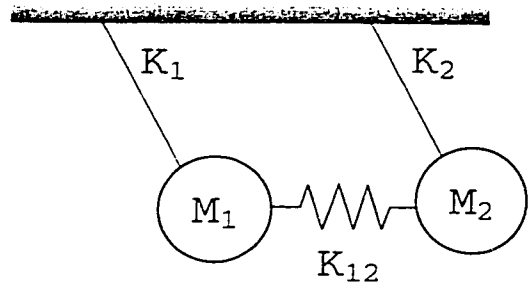

FIGURE 3.4 Coupled spring-mass resonators in-phase mode.

If the masses are displaced an equal distance in opposite directions, as shown in Figure 3.5, the spring K_{12} will be stretched, but there will be no displacement at the exact center of the spring.

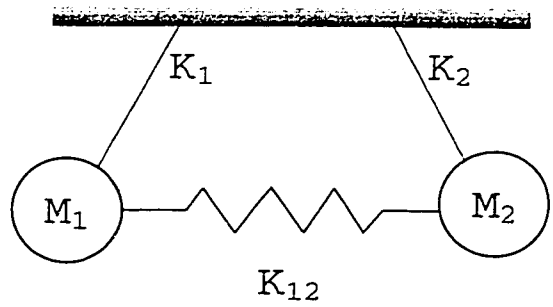

FIGURE 3.5 Coupled-spring-mass resonators out-of-phase mode f_2.

When we release the masses, the spring is alternately compressed and expanded during each cycle, but the center of the spring remains stationary, that is, it becomes a node [4]. The frequency of the coupled resonators remain constant at a value f_2, as if the system were composed of the single mass and two springs K_1 and $2K_{12}$. The coupling spring is one-half the length of the original and therefore has twice the stiffness $2K_{12}$ [4]. The second resonance frequency is a function of sum of the two spring stiffnesses (note the assumption $K_1=K_2$ and $M_1=M_2$) and therefore [4]

$$f_2 = \frac{1}{2\pi}\sqrt{\frac{K_1 + 2K_{12}}{M_1}} \tag{3.2}$$

Thus, the two-resonator filter has two natural resonances, f_1 and f_2. It is important to note that at frequency f_1 the displacements of the masses are in phase, whereas at frequency f_2, the displacements are 180 degrees out of phase. In higher order mechanical filters there is an additional natural resonance for each resonator added [4]. For example, in an n^{th} order MEMS filter there is n distinct natural resonances.

As illustrated in Figure 3.6, each of the above vibration modes (f_1 and f_2) corresponds to a distinct peak in the force-to-displacement frequency characteristic and to a distinct physical mode shape of the coupled mechanical resonator system. The relative spacing between these mode peaks determines the passband of the eventual filter.

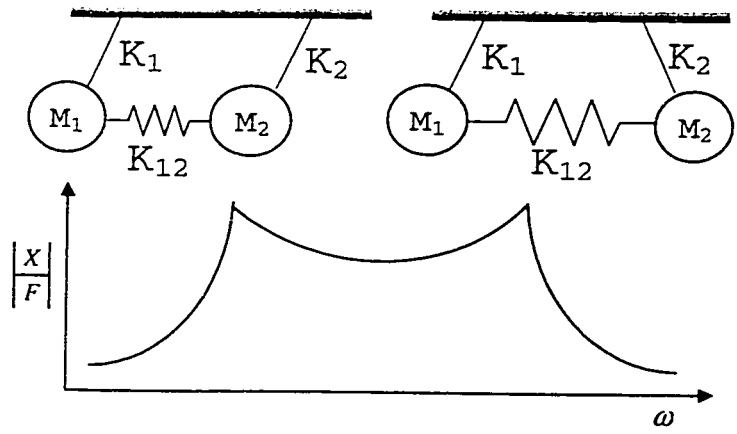

FIGURE 3.6 Mode shapes of a two-resonator MEMS filter and their corresponding frequency peaks.

The resonators and coupling spring can be combined to realize a specified filter bandwidth. The general procedure for designing a MEMS bandpass filter involves two main steps (not necessarily in this order):

1. Design of mechanical resonators with resonance frequencies at or near f_0 and with reasonable stiffnesses K_i and
2. Design of coupling springs with appropriate values of stiffness K_{ij} to achieve a desired bandwidth.

3.2 MEMS RESONATOR DESIGN

The constituent resonators in MEMS filters are preferably designed to be identical, with identical spring dimensions and resonance frequencies. For such designs, the resonance frequency of the overall filter is approximately equal to the resonance frequency f_0 of the resonators. Assuming given values for structural material thickness h, suspension width W_i, and length L_i (the length of the inner and outer beams are the same) are specified resulting in resonator stiffnesses

$$K_i = 2Eh\left(\frac{W_i}{L_i}\right)^3 \tag{3.3}$$

The effective mass M_i, found at the shuttle location can now be written as

$$M_i = M_s + \frac{1}{4}M_t + \frac{12}{35}M_b \tag{3.4}$$

where Ms, Mt and Mb are the masses at the shuttle, trusses, and beams respectively. The natural resonant frequency response of this resonator is approximated through ODEs as

$$f_0 = \frac{1}{2\pi}\sqrt{\frac{k_i}{m_i}} \tag{3.5}$$

MEMS resonators are adequate for implementation of high performance, small percent bandwidth filters. Figure 3.7 shows the spectrum response of a single resonator. The design of the mechanical properties can significantly

change the characteristic of the filter spectrum. The response shown in Figure 3.7 was realized with a resonator beam length L = 150 μm, and width W = 2 μm resulting in K = 1.602 N/m. The equivalent mass of the resonator is M = $9.62X10^{-11}$ Kg. The center frequency is seen to be 20.5 kHz. This value of center frequency corresponds very well with Equations 3.3, 3.4 and 3.5.

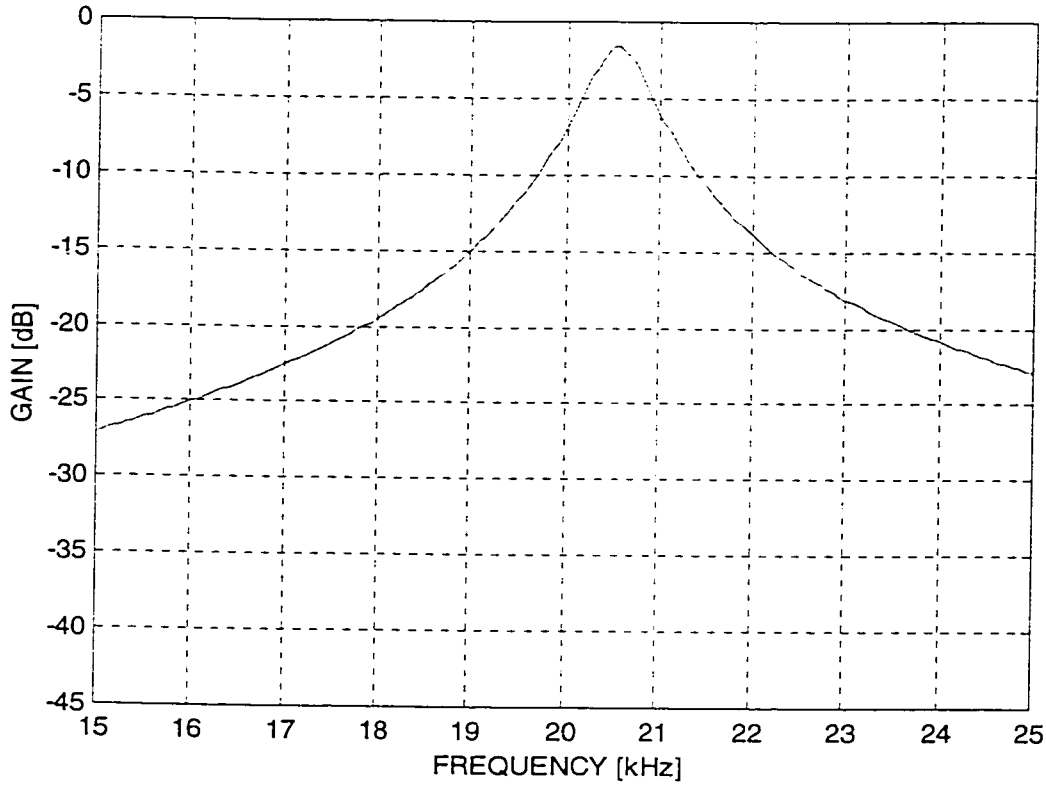

FIGURE 3.7 Frequency characteristic for a single comb-transduced micromechanical resonator using SPICE.

3.3 COUPLING SPRING DESIGN

The placement of the vibration peaks in the frequency characteristic – and thus, primarily the stiffness of the coupling spring K_{12} and the constituent resonators at their coupling locations K_1 and K_2 determine the passband of the

eventual filter. In particular, for a filter with center frequency f_0 and 3dB bandwidth BW_{3dB}, these stiffnesses must satisfy the expression [4], [6]

$$K_{ij} = K_i k_{ij} \frac{BW_{3dB}}{f_0}\bigg|_{K_i = K_j} \tag{3.6}$$

where k_{ij} is a normalized coupling coefficient derived from a ratio of resonance and 3-dB cutoff frequencies and easily found in filter handbooks [4]. Note from Equation 3.6 that the filter bandwidth is not dependent on the absolute values of resonator and coupling beam stiffness; rather, their ratio K_{ij}/K_i dictates bandwidth. Figure 3.8 shows the frequency characteristic of two resonators, with the above dimensions, coupled by a square truss coupling spring. The coupling spring length is $L_{12} = 175$ μm, and width $W_{12} = 1$ μm resulting in $K_{12} = 0.063$N/m. The center frequency is seen to be 21 kHz. This result corresponds well with equations 3.1 and 3.2. The shape factor and stopband rejection of the two-resonator MEMS filter shows improvement compared to a single resonator filter.

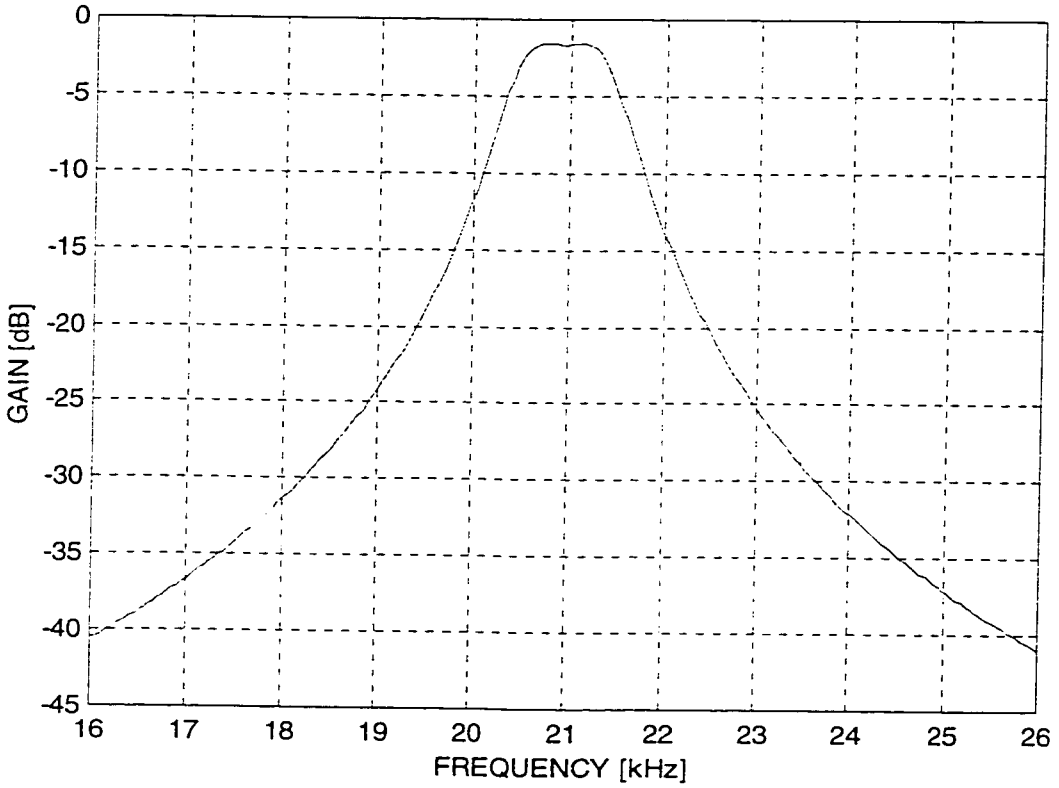

FIGURE 3.8 Frequency characteristic for a two-resonator comb-transduced micromechanical filter using SPICE.

Characteristics	Two-resonator Filter
Center frequency (f_0) [kHz]	21.0
3dB bandwidth (BW_{3dB}) [kHz]	1.04
20dB bandwidth (BW_{20dB}) [kHz]	3.07
Fractional bandwidth (BW_{3dB} / f_0)	4.95
Passband ripple [dB]	0.2
Shape factor (BW_{20dB} / BW_{3dB})	2.95
Quality factor (f_0 / BW_{3dB})	20.2

TABLE 3.1 Characteristics of two-resonator MEMS filter.

3.4 THE PROGRAMMABLE STRUCTURE

The above details the nominal frequency response of a two-resonator MEMS bandpass filter. The programmability of such a filter can be incurred by the effect that the electrical spring constant has on these two mode peaks.

From Equations 3.1 and 3.2 we can see that changes to stiffness of the two resonators, K_1 and K_2, due to the parallel plate structures on the individual resonators will change the center frequency of the two-resonator filter. These resonator stiffnesses vary with the application of the tuning voltage which is applied to the parallel-plate structures of that particular resonator.

Figure 3.9 shows the frequency programmability of a single resonator. The relevant dimensions of this graph are found in the above single resonator design, and are summarized in Table 3.2. It can be seen by the graph that the values of center frequency decrease slowly with increasing voltage, dropping down to zero at approximately 37 Volts. It seems, by looking at the ODE model, that the programmability of the filter can yield as much as 95%. These results will need to be substantiated with FEA.

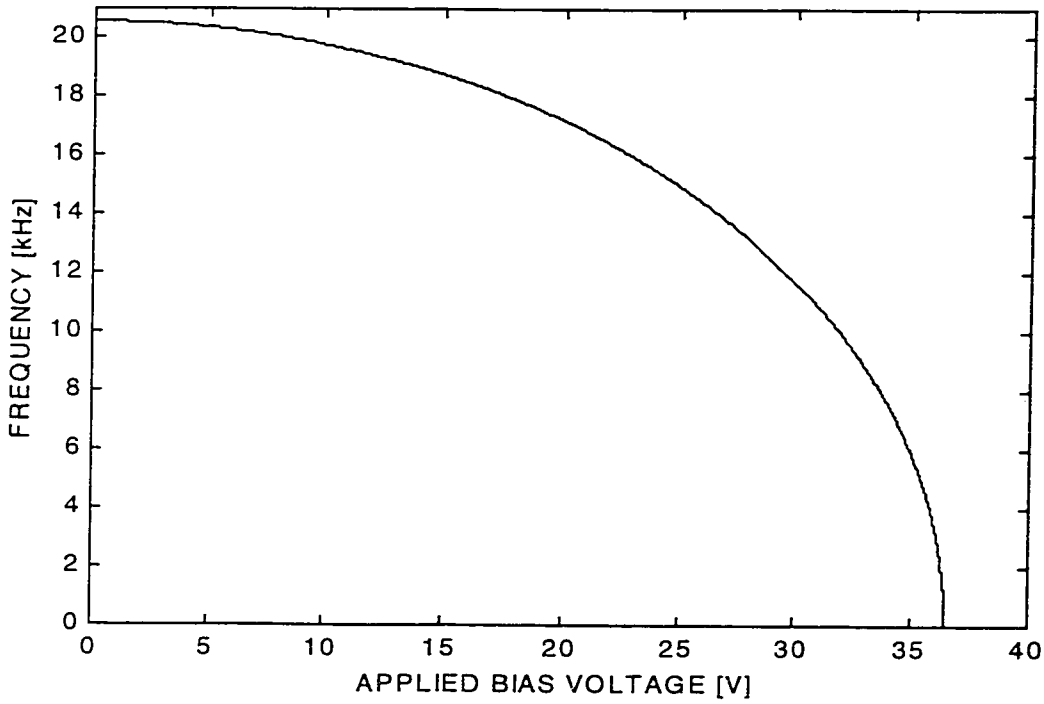

FIGURE 3.9 Predicted frequency variation for single resonator designed above.

Furthermore, from the diagram in Figure 3.6, it can be seen that when the resonators are vibrating in phase, they will be subjected to the electrical spring constant due to the parallel-plate structures on the spring. When the resonators are vibrating 180 degrees out of phase, this mode is not affected since the center of the spring remains motionless. This will change the filter bandwidth because mode f_1 will change due to the electrical spring constant and mode f_2 remains the same. The approximation that the spring connecting the two resonators will behave as a rigid body at mode f_1 will help us to theoretically predict how the filter's bandwidth changes with voltage. Given the assumption that the two resonators have identical spring constants (both mechanical and electrostatic) and masses, mode peak f_1 can be modeled as

$$f_1 = \frac{1}{2\pi}\sqrt{\frac{K_1 - K_{e1} - K_{ecs}}{M_1}} \tag{3.7}$$

and mode peak f_2 can be modeled as

$$f_2 = \frac{1}{2\pi}\sqrt{\frac{K_1 - K_{e1} + 2K_{12}}{M_1}} \tag{3.8}$$

where K_1 and K_{12} are the nominal mechanical stiffness and K_{e1} and K_{ecs} are the electrostatic stiffness due to the DC voltage bias on resonator and coupling spring, respectively. Figure 3.10 shows the predicted change between these two mode peaks versus applied bias voltage V_{ts}.

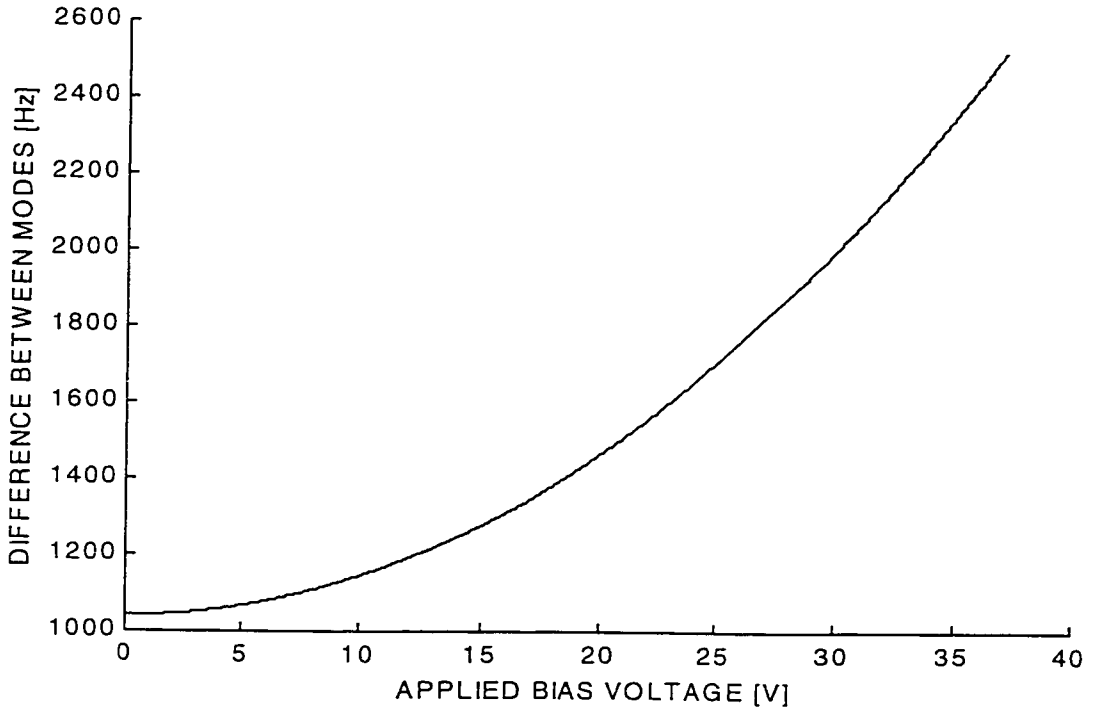

FIGURE 3.10 Predicted variation is filter's frequency versus applied bias voltage.

The mechanical equivalent model for the programmable filter used lumped parameters to approximate the frequency characteristics of the filter. Use of classical methods is probably the best way to analyze simple structures; nevertheless, their use with more complex model may be misleading. In such

cases the best alternative is usually a solution obtained with the finite element method.

3.5 COMPLETE FILTER DESIGN SUMMARY

The parameters derived above along with other relevant parameters for this filter are summarized in Table 3.2. All plots in this chapter were generated using the electrical analogous circuit modeled in section 2.2. Given the filter specifications a circuit simulation netlists (network listings) for these MEMS filters were constructed.

Parameter	Designed/Simulated
Resonator Stiffness @ Shuttle, K	1.60237 N/m
Resonator Mass @ Shuttle, M	9.61957×10^{-11} Kg
No. of Drive/Sense Fingers Per Side, N	10
Drive/Sense Comb-Finger Gap Spacing, d	2 μm
Drive/Sense Comb-Finger Overlap, L	10 μm
Structural Layer Thickness, h	2 μm
Young's Modulus, E	169 GPa
Density of Polysilicon, ρ	2300 kg/m^3
Coupling Beam Length, L_{12}	175 μm
Filter DC-Bias, V_b	10 V
No. of Tuning Fingers per resonator, N_{tr}	4
Tuning Finger Gap Spacing for resonator, d_{tr}	2 μm
Tuning Finger Overlap Length for resonator, L_{tr}	10 μm
No. of Tuning Fingers for Spring, N_{ts}	4
Tuning Finger Gap Spacing for Spring, d_{ts}	2 μm
Tuning Finger Overlap Length for Spring, L_{ts}	10 μm

TABLE 3.2 Programmable two-resonator MEMS filter design summary.

3.6 DISCUSSION

Chapter 3 begins with a description of the filter passband. The two mode peaks that determine the filter's center frequency and bandwidth are

related through equations to the spring constants and masses of the filter resonators and coupling spring. Filter parameters are chosen (summarized in Table 3.2) and will be used in subsequent Chapters. The nominal filter response was generated using electro-mechanical analogies discussed in Chapter 1. The filter programmability, both in center frequency and bandwidth, is predicted by ODEs and then plotted versus voltage. The filter's center frequency, by looking at the graph, can yield a programmability of as much as 95%. Similarly, the filter's bandwidth shows this very generous programmable range. These results will need to be substantiated with FEA.

4

DYNAMIC SYSTEM MODELING USING SIMULINK

Any continuous time system can be described using ordinary differential equations (ODEs). Moreover any continuous time system can be modeled in Simulink. The MEMS bandpass filter is such a system. Figure 4.1 shows the Simulink model of the MEMS bandpass filter.

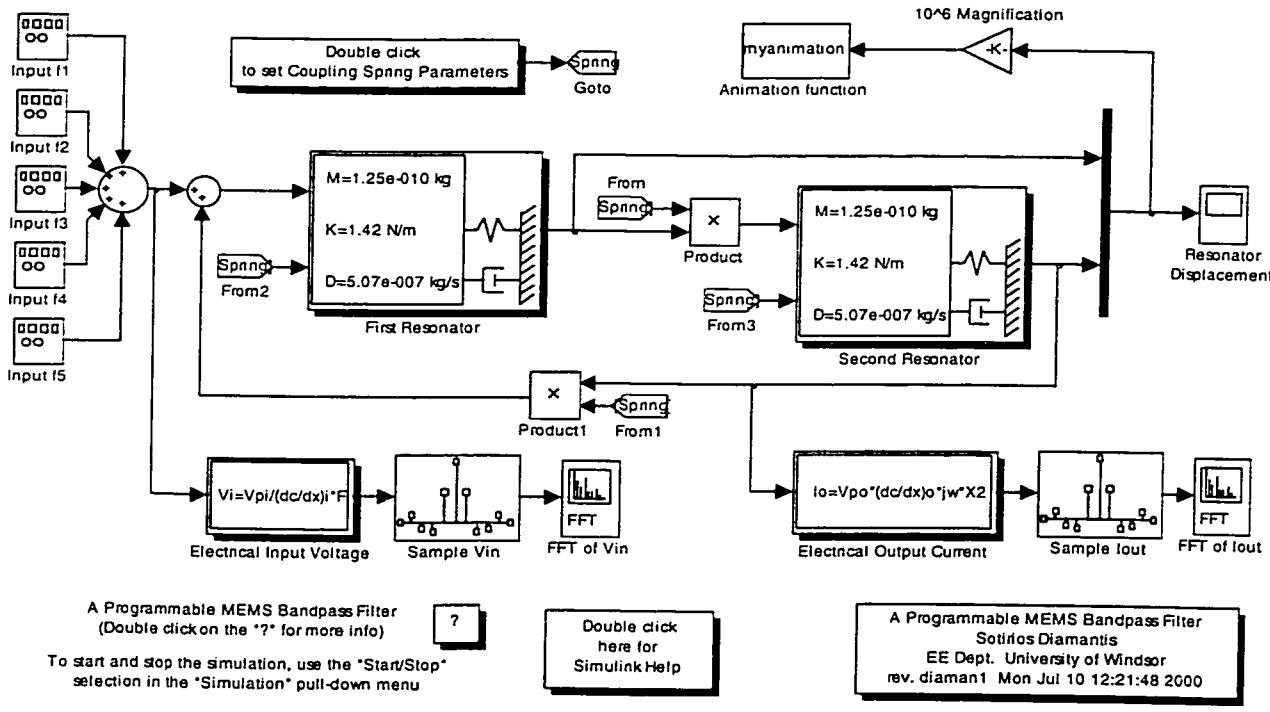

FIGURE 4.1 Simulink model of the MEMS bandpass filter.

This chapter focuses on explaining the model of Figure 4.1. More specifically, section 4.1 describes how to model the resonators using hierarchical blocks called masked subsystems and section 4.2 discusses S-Function based graphical animations.

4.1 MASKED SUBSYSTEMS

As models grow larger and more complex, they can easily become difficult to understand and maintain. Subsystems solve this problem by breaking a large model into a hierarchical set of smaller models. Subsystems can be viewed as reusable model components. Suppose that we wish to compare several different mass, spring and damping designs using the same second order MEMS filter model. Rather than building a complete new block diagram each time, it is more convenient to enter the block properties such as mass, spring and damping that model the new system. Not only does this save time building the model, but it also ensures software reuse. An important advantage of software reuse is that once we have verified that a subsystem is correct, we don't have to repeat the testing and debugging process each time we use the subsystem in a new model. It is for this reason that we are using masked subsystems to model the resonators and spring in our Simulink model.

Masking permits us to treat a subsystem as if it were a simple block. A masked block may have a custom icon, and it may also have a dialog box in which configuration parameters are entered in the same way parameters are entered for blocks in the Simulink block libraries.

Consider the model shown in Figure 4.1. Double-clicking the block labeled Resonator 1, which is shown in Figure 4.2 for clarity, opens the dialog box shown in Figure 4.3.

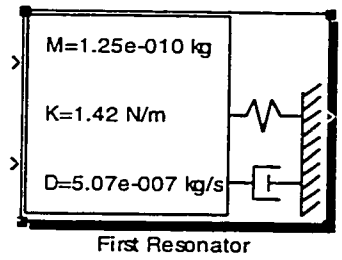

FIGURE 4.2 First resonator masked subsystem block.

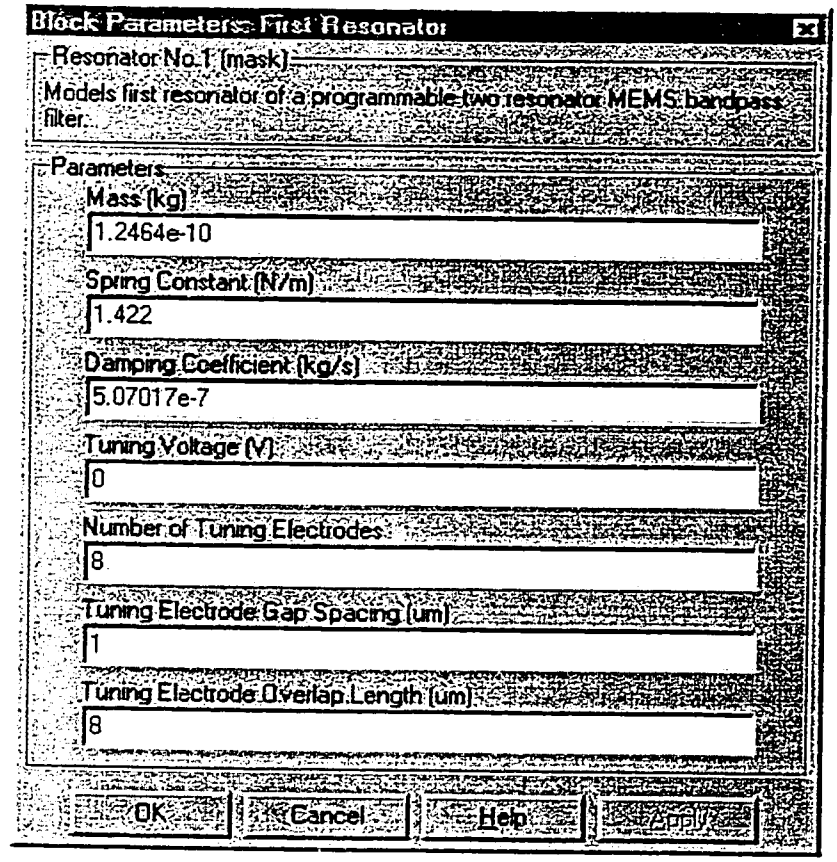

FIGURE 4.3 Dialog box modeling the first resonator of the MEMS filter.

Instead of opening the dialog box for each Gain block and each Integrator to set the block parameters, we can enter all the parameters for each subsystem in the subsystem's dialog box.

Simulink allows us to design custom icons for masked blocks. To create the custom icon drawing for the first resonator the following commands must be entered in the Mask Editor Icon page:

```
plot([0.2,0.8,0.8,0.2,0.2],[0.2,0.2,0.8,0.8,0.2])
plot(0.8+[0,0.05,0.075,0.1,0.125,0.15,0.22],[0.5,0.5,0.55,0.45,0.55,0.5,0.5])
plot(0.8+[0,0.075],[0.3,0.3]), plot(0.8+[0.075,0.075],[0.25,0.35])
plot(0.875+[0,0.075],[0.35,0.35]), plot(0.875+[0.0.075],[0.25,0.25])
plot(0.8+[0.12,0.12],[0.275,0.325]), plot(.92+[0,0.1],[0.3,0.3])
plot([1.02,1.02],[0.2,0.575])
plot([1.02,1.07],[0.2,0.24]), plot([1.02,1.07],[0.24,0.28])
plot([1.02,1.07],[0.28,0.32]), plot([1.02,1.07],[0.32,0.36])
plot([1.02,1.07],[0.36,0.40]), plot([1.02,1.07],[0.40,0.44])
plot([1.02,1.07],[0.44,0.48]), plot([1.02,1.07],[0.48,0.52])
plot([1.02,1.07],[0.52,0.56]), plot([1.02,1.07],[0.56,0.60]).
```

To display the mass, spring and damping of resonator 1 on the icon, we must add the following commands to the Initialization Commands Field on the Initialization page of the Mask Editor:

```
m_label=sprintf('M=%1.2e kg', M1);
k_label=sprintf('K=%1.2f N/m', K1);
d_label=sprintf('D=%1.2e kg/s', D1);
```

and enter the following commands in the Drawing Commands field of the Icon page:

```
text(0.275,0.7,m_label);
text(0.275,0.5,k_label);
text(0.275,0.3,d_label);.
```

In order to model the system, it is necessary to write the equations of motion (ODEs) of the nominal frequency response, and apply to that the programmability of the filter through the electro-spring.

$$M_1 \ddot{X}_1 + D_1 \dot{X}_1 + (K_1 + K_{12})X_1 - K_{12}X_2 = F$$

or, solving for $\ddot{X}_1$;

$$\ddot{X}_1 = \frac{F}{M_1} - \frac{D_1}{M_1}\dot{X}_1 - \frac{(K_1 + K_{12})}{M_1}X_1 + \frac{K_{12}}{M_1}X_2 \qquad (4.1)$$

and

$$M_2 \ddot{X}_2 + D_2 \dot{X}_2 + (K_2 + K_{12})X_2 - K_{12}X_1 = 0$$

and simplifying for $\ddot{X}_2$;

$$\ddot{X}_2 = -\frac{D_2}{M_2}\dot{X}_2 - \frac{(K_2 + K_{12})}{M_2}X_2 + \frac{K_{12}}{M_2}X_1 \tag{4.2}$$

Equation 4.1 is used to depict resonator 1 using block diagram components. The subsystem for the first resonator is configured to use masked block variables and illustrated in Figure 4.4. A similar subsystem is used to model the second resonator based on Equation 4.2.

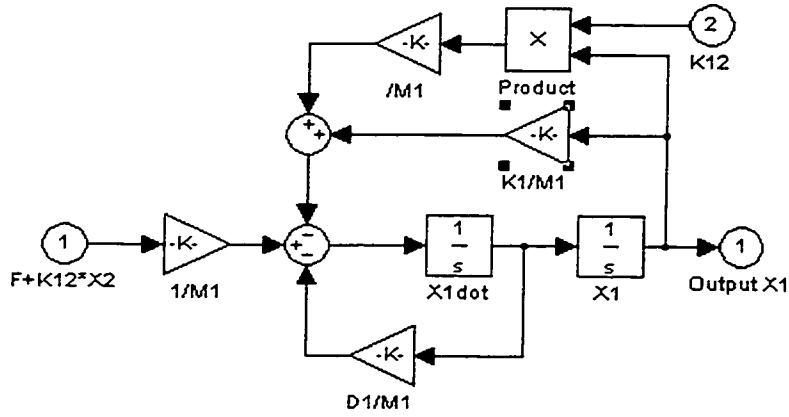

FIGURE 4.4 Masked subsystem block for first resonator.

4.2 GRAPHICAL ANIMATION

Graphical animations can make it easier to visualize the process being simulated. As the simulation progresses, the resonators and spring move to graphically depict the state of the simulation. This animation makes it much easier to visualize the motion of the MEMS bandpass filter.

S-Function-based animations are S-Functions (special MATLAB functions that permit the system dynamics to be expressed as equations) that have no states and no outputs. Therefore, they are custom sinks. An animation S-Function has two main parts: initialization and update. During initialization, the

figure window is created and the animation objects are prepared. During updates, the properties of the animation objects are changed as a function of the S-Function block inputs.

The figure initialization logic starts by creating the figure associated with the current block using the following MATLAB statements:

```
mymodel = findobj('Type','figure','Name','mymodel Animation');
```

The animation figure is redrawn using the MATLAB graphics commands included, under case flag==0, in Listing 4.1.

The last step in figure initialization is to save the handles of the elements that will move during the simulation. The technique used here to save these elements is to group them into a single MATLAB variable, and store that variable in the S-Function block UserData as shown below.

```
hndl=plot(x,y,'y','EraseMode','background','LineWidth',2);
set(gca,'UserData',hndl);
```

The animation S-Function is treated as a discrete block because we set the sample time to a positive number. Simulink will execute the S-Function at predetermined sample times defined under case flag==2. The update function reads from the S-Function block UserData the handles of the graphics objects that will change as shown below.

```
hndl=get(gca,'UserData');
```

The new displacement values of the objects are updated using the set command:

```
set(hndl,'XData',x);
```

Listing 4.1 shows the S-Function based animation, and the animation figure is shown in Figure 4.5.

```
function [sys,x0]=myanimation(t,x,u,flag,ts);
% MYANIMATION S-function for animating the motion of a programmable MEMS bandpass filter

% Sotirios Diamantis, August 2000
% Electrical & Computer Engineering, University of Windsor

global xR2T xR2B xSpring mymodel

if flag==2,
  if any(get(0,'Children')==mymodel),
   if strcmp(get(mymodel,'Name'),'mymodel Animation'),
    set(0,'currentfigure',mymodel);
      hndl=get(gca,'UserData');
          x=[-xR2T+u(1); ...
              -xR2B(1:3,1)+u(1)/2; -xR2B(4,1); -xR2B(5:7,1)+u(1)/2; ...
              -xR2B(8,1); -xR2B(9:13,1)+u(1)/2; -xR2B(14:21,1)+u(1); ...
              -xR2B(22:24,1)+u(1)/2; -xR2B(25,1); -xR2B(26:28,1)+u(1)/2; ...
              -xR2B(29,1); -xR2B(30:34,1)+u(1)/2; -xR2B(35:40,1)+u(1); ...
               xSpring(1:5,1)+u(2)/2; xSpring(6,1)+u(2); xSpring(7:11,1)+u(2)/2; ...
               xSpring(12,1)+u(1); xSpring(13:14,1)+u(2)/2; xSpring(15,1)+u(2); ...
               xR2T+u(2); ...
               xR2B(1:3,1)+u(2)/2; xR2B(4,1); xR2B(5:7,1)+u(2)/2; ...
               xR2B(8,1); xR2B(9:13,1)+u(2)/2; xR2B(14:21,1)+u(2); ...
               xR2B(22:24,1)+u(2)/2; xR2B(25,1); xR2B(26:28,1)+u(2)/2; ...
               xR2B(29,1); xR2B(30:34,1)+u(2)/2; xR2B(35:40,1)+u(2)];
        set(hndl,'XData',x);
       drawnow;
   end
  end
  sys=[];

elseif flag == 4 % Return next sample hit

  % ns stores the number of samples
  ns = t/ts;

  % This is the time of the next sample hit.
  sys = (1 + floor(ns + 1e-13*(1+ns)))*ts;

elseif flag==0,

  % Initialize the figure for use with this simulation
   aminit('mymodel Animation');
     mymodel = findobj('Type','figure','Name','mymodel Animation');
  axis([-90 90 -225 225]);
  hold on;
  zoom on;

  xyR2T= [ ...
        5       0;       10       0;       10       84;       15       84;
```

```
        15      40;     20      40;     20      10;     44      10;
        44      40;     49      40;     49      84;     54      84;
        64      84;     54      84;     54      72;     64      72;
        54      72;     54      60;     64      60;     54      60;
        54      48;     64      48;     54      48;     54      36;
        64      36;     54      36;     54      24;     64      24;
        54      24;     54      12;     64      12;     54      12;
        54      0;      64      0;      54      0;      54      -12;
        64      -12;    54      -12;    54      -24;    64      -24;
        54      -24;    54      -36;    64      -36;    54      -36;
        54      -48;    64      -48;    54      -48;    54      -60;
        64      -60;    54      -60;    54      -72;    64      -72;
        54      -72;    54      -84;    64      -84;    49      -84;
        49      -40;    44      -40;    44      -5;     20      -5;
        20      -40;    15      -40;    15      -84;    10      -84;
        10      84;     15      84;     15      40;     20      40];

xyR2B= [ ...
        20      170;    20      150;    28      150;    28      40;
        28      170;    28      150;    36      150;    36      40;
        36      170;    36      150;    44      150;    44      170;
        44      150;    44      40;     49      40;     49      84;
        54      84;     54      -84;    49      -84;    49      -40;
        44      -40;    44      -170;   44      -150;   36      -150;
        36      -40;    36      -170;   36      -150;   28      -150;
        28      -40;    28      -170;   28      -150;   20      -150;
        20      -170;   20      -150;   20      -40;    15      -40;
        15      -84;    10      -84;    10      0;      5       0];

xySpring= [ ...
        -5      200;    -5      180;    5       180;    5       200;
        5       180;    5       0;      5       -200;   5       -180;
        -5      -180;   -5      -200;   -5      -180;   -5      0;
        -5      180;    5       180;    5       0];

xR2T=xyR2T(:,1);
yR2T=xyR2T(:,2);
xR2B=xyR2B(:,1);
yR2B=xyR2B(:,2);
xSpring=xySpring(:,1);
ySpring=xySpring(:,2);

x=[-xR2T; -xR2B; xSpring; xR2T; xR2B];
y=[yR2T; yR2B; ySpring; yR2T; yR2B];

% Draw nail down points
        % Resonator anchors
```

```
plot([27 37 37 27 27],[25 25 40 40 25],'y', ...
     [27 37 37 27 27],-[25 25 40 40 25],'y', ...
     -[27 37 37 27 27],[25 25 40 40 25],'y', ...
     -[27 37 37 27 27],-[25 25 40 40 25],'y', 'LineWidth',2);
plot([28 36 36 28 28],[27 27 38 38 27],'k', ...
     [28 36 36 28 28],-[27 27 38 38 27],'k', ...
     -[28 36 36 28 28],[27 27 38 38 27],'k', ...
     -[28 36 36 28 28],-[27 27 38 38 27],'k','LineWidth',1);
       % Drive and Sense Fixed Fingers
plot([59 69 69 59 69 69],[90 90 78 78 78 66],'y', ...
     [59 69 69 59 69 69],[66 66 54 54 54 42],'y', ...
     [59 69 69 59 69 69],[42 42 30 30 30 18],'y', ...
     [59 69 69 59 69 69],[18 18 6 6 6 -6],'y', ...
     [59 69 69 59 69 69],-[6 6 18 18 18 30],'y', ...
     [59 69 69 59 69 69],-[30 30 42 42 42 54],'y', ...
     [59 69 69 59 69 69],-[54 54 66 66 66 78],'y', ...
     [59 69 69 59 74],-[78 78 90 90 90],'y', ...
     [74 74 69],[-90 90 90],'y', 'LineWidth',2);
plot(-[59 69 69 59 69 69],[90 90 78 78 78 66],'y', ...
     -[59 69 69 59 69 69],[66 66 54 54 54 42],'y', ...
     -[59 69 69 59 69 69],[42 42 30 30 30 18],'y', ...
     -[59 69 69 59 69 69],[18 18 6 6 6 -6],'y', ...
     -[59 69 69 59 69 69],-[6 6 18 18 18 30],'y', ...
     -[59 69 69 59 69 69],-[30 30 42 42 42 54],'y', ...
     -[59 69 69 59 69 69],-[54 54 66 66 66 78],'y', ...
     -[59 69 69 59 74],-[78 78 90 90 90],'y', ...
     -[74 74 69],[-90 90 90],'y', 'LineWidth',2);
plot([70 73 73 70 70],[87 87 -87 -87 87],'k', ...
    -[70 73 73 70 70],[87 87 -87 -87 87],'k', 'LineWidth',1);
       % Tuning Fixed Fingers
plot([16 16 24 24],[158 178 178 158], 'm', ...
     [24 32 32 32],[178 178 158 178], 'm', ...
     [32 40 40 40],[178 178 158 178], 'm', ...
     [40 48 48 48],[178 178 158 178], 'm', ...
     [48 48 16 16],[178 188 188 178], 'm', 'LineWidth',2);
plot([16 16 24 24],-[158 178 178 158], 'm', ...
     [24 32 32 32],-[178 178 158 178], 'm', ...
     [32 40 40 40],-[178 178 158 178], 'm', ...
     [40 48 48 48],-[178 178 158 178], 'm', ...
     [48 48 16 16],-[178 188 188 178], 'm', 'LineWidth',2);
plot(-[16 16 24 24],[158 178 178 158], 'r', ...
     -[24 32 32 32],[178 178 158 178], 'r', ...
     -[32 40 40 40],[178 178 158 178], 'r', ...
     -[40 48 48 48],[178 178 158 178], 'r', ...
     -[48 48 16 16],[178 188 188 178], 'r', 'LineWidth',2);
plot(-[16 16 24 24],-[158 178 178 158], 'r', ...
     -[24 32 32 32],-[178 178 158 178], 'r', ...
     -[32 40 40 40],-[178 178 158 178], 'r', ...
```

```
        -[40 48 48 48],-[178 178 158 178], 'r', ...
        -[48 48 16 16],-[178 188 188 178], 'r', 'LineWidth',2);
    plot([-9 -9 0 0 0 9 9],[188 208 208 188 208 208 188], 'b', ...
        [9 9 -9 -9],[208 218 218 208], 'b', 'LineWidth',2);
    plot([-9 -9 0 0 0 9 9],-[188 208 208 188 208 208 188], 'b', ...


        [9 9 -9 -9],-[208 218 218 208], 'b', 'LineWidth',2);
    plot([47 47 17 17 47],[180 186 186 180 180], 'k', ...
        [47 47 17 17 47],-[180 186 186 180 180], 'k', ...
       -[47 47 17 17 47],[180 186 186 180 180], 'k', ...
       -[47 47 17 17 47],-[180 186 186 180 180], 'k', ...
        [8 8 -8 -8 8],[210 216 216 210 210],'k', ...
        [8 8 -8 -8 8],-[210 216 216 210 210],'k', 'LineWidth',1);

    hndl=plot(x,y,'y','EraseMode','background','LineWidth',2);
    set(gca,'UserData',hndl);
    %set(gcf,'Color','w');

    sys=[0 0 0 2 0 0];
    x0=[];
end;
```

LISTING 4.1 MEMS filter S-Function based animation.

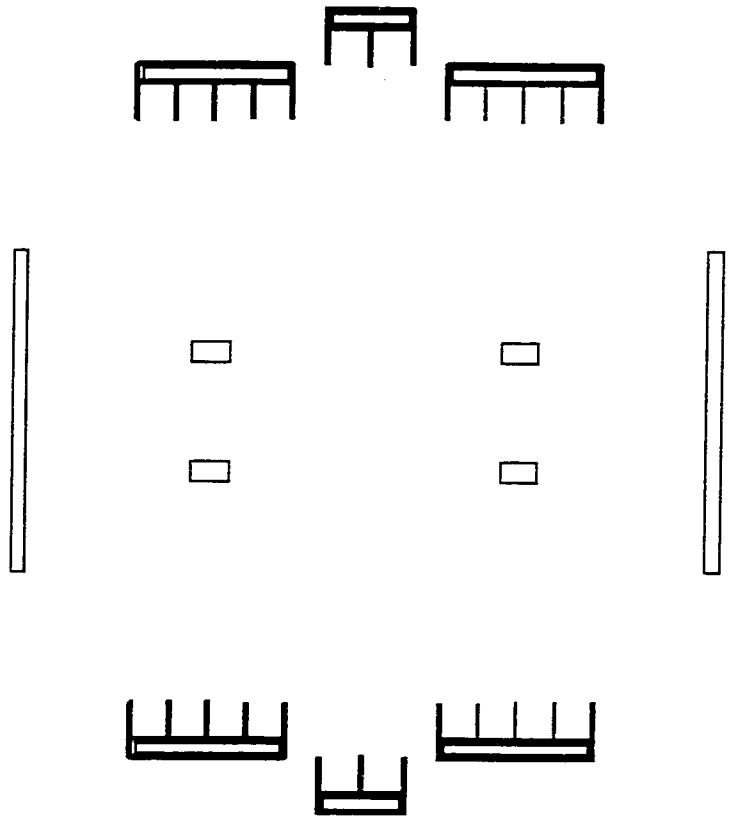

FIGURE 4.5 MEMS filter S-Function animation figure.

5

FABRICATION & SIMULATION USING INTELLISUITE

There are a large number of fabrication technologies capable of realizing micromechanical structures. This chapter begins with a brief overview of the specific technique used in this work: surface micromachining. This technique involves a sequence of depositions and patternings to achieve a structure in which the film-to-be-suspended sits upon a sacrificial film, which is exposed to the surface and can be accessed by etchants. A sacrificial etch then removes the sacrificial layer, freeing the structure in the process. Recently, this technique has been used to fabricate a wide variety of MEMS devices, including MEMS bandpass filters [1, 6, 14].

Three-dimensional FEA simulation results are necessary to accurately predict the frequency tuning properties of the programmable MEMS filter. The programmable frequency ranges of both the individual resonators and the two-resonator filter will be demonstrated by a 3-D FEA simulation with IntelliSuite software. A comparison of values computed using lumped parameter methods (ODEs) and distributed parameter methods (3-D FEA) will be carried out.

5.1 MEMS FILTER FABRICATION

Figures 5.1 through 5.10 show cross-sections of the fabrication of a microelectromechanical bandpass filter at successive stages of fabrication. These figures show cross-section views of a suspended electrode, in order to describe the surface-micromachining of the filter's polycrystalline silicon structure. Appendix B is a step-by-step outline of the IntelliSuite process. Here, we will take a closer look at the most important steps of the process.

The starting material for the fabrication process is a silicon substrate as shown in Figure 5.1.

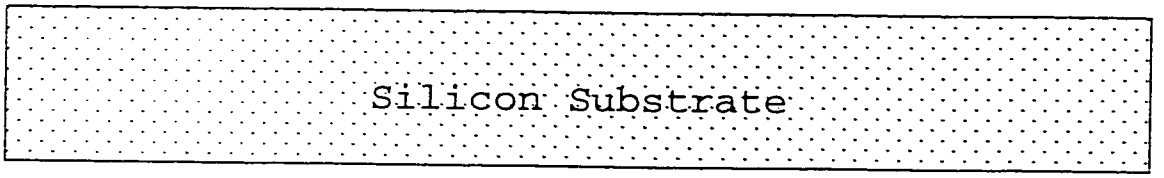

FIGURE 5.1 The silicon substrate is the starting material in the fabrication process.

The first oxide layer above the silicon substrate serves as a structural buffer that reduces the capacitance from structure to substrate. The capacitance from structure to substrate may seriously degrade the performance of filters based upon micromechanical resonators. Thus, this oxide layer should be as thick as possible [14]. The substrate is oxidized as shown in Figure 5.2.

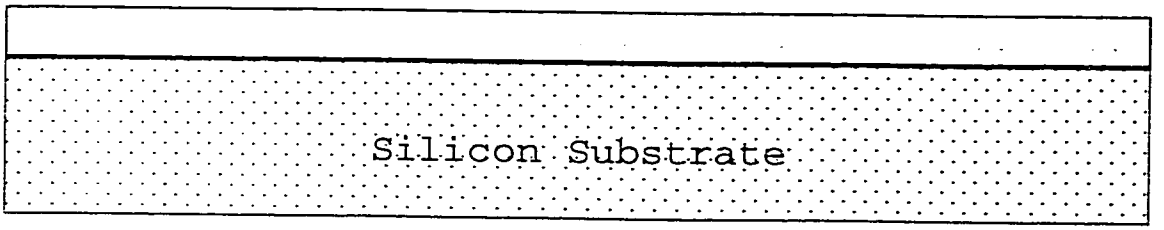

FIGURE 5.2 An oxide layer is formed above the silicon substrate.

The silicon nitride layer deposited directly above the oxide protects the oxide from sacrificial etchant, which is most often hydrofluoric acid. The etch rate selectivity of oxide to silicon nitride is very large for all available concentrations of hydrofluoric acid [14]. Nitride is deposited by low-pressure chemical vapor deposition (LPCVD) on the oxide layer as shown in Figure 5.3.

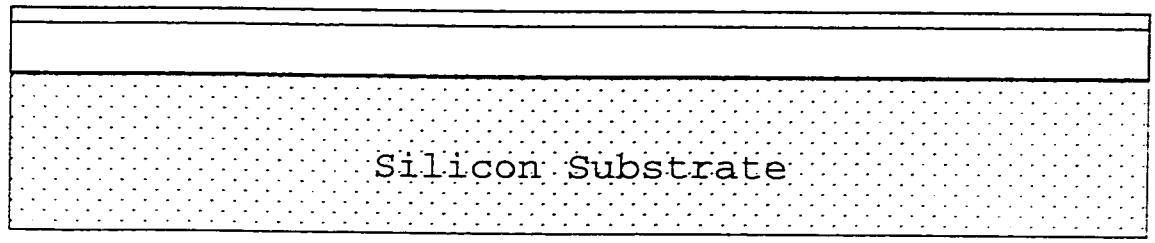

FIGURE 5.3 Nitride is deposited by LPCVD on the oxide layer.

The thin (300 nm) layer of polycrystalline silicon is deposited over the silicon nitride layer as shown in Figure 5.4. This layer serves as a ground plane connected to the resonator, which prevents the resonator from pulling into the substrate due to voltage differences [14].

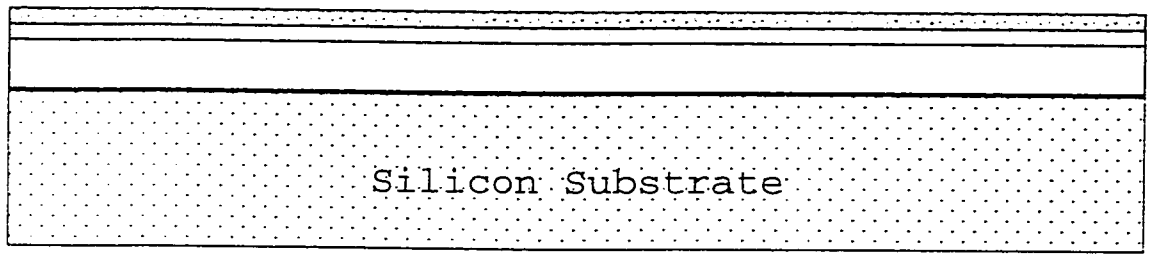

FIGURE 5.4 A thin layer of polycrystalline silicon is deposited over the silicon nitride layer.

The above polycrystalline silicon layer is patterned by laying a first mask and performing a SF6-plasma dry etch as shown in Figure 5.5.

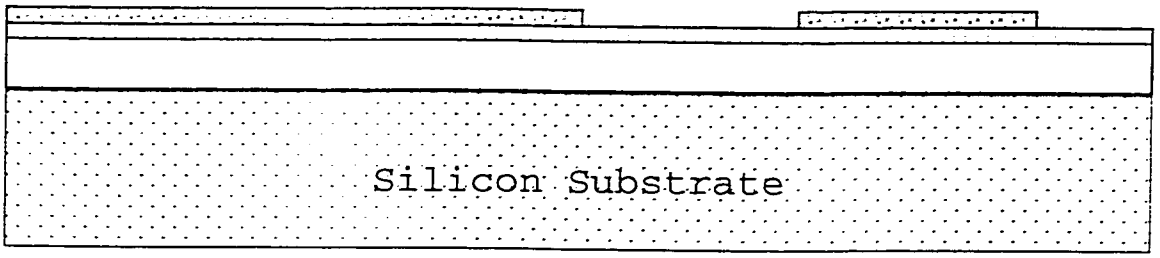

FIGURE 5.5 Laying the first mask and etching, patterns the polycrystalline silicon layer.

The next layer of oxide, depicted in Figure 5.6, is placed onto this first layer of polycrystalline silicon (polySi). This layer of oxide, between the first layer of polycrystalline silicon and the structural polysilicon, serves as a sacrificial oxide layer. It temporarily supports the structural polySi until the sacrificial etch.

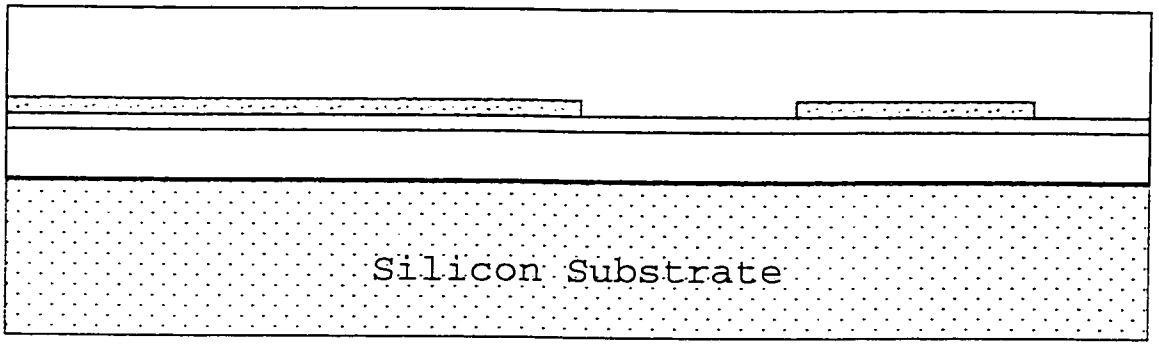

FIGURE 5.6 A sacrificial oxide layer is deposited between the first polysilicon layer below and the structural polysilicon above, and serves to temporarily support the structural polysilicon.

Subsequently, wells are made in the sacrificial oxide layer which extend down to portions of the polysilicon by use of a second mask followed by a wet etch, as shown in Figure 5.7.

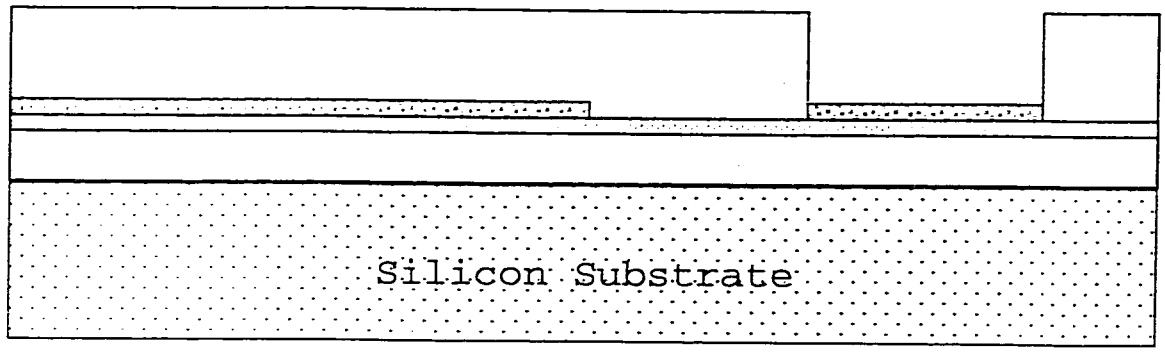

FIGURE 5.7 Wells are made in the sacrificial oxide layer that extend down to portion of the polysilicon.

A second layer of polycrystalline silicon is deposited by LPCVD, forming the structural polysilicon layer. This structural polysilicon is anchored to the first polysilicon layer and has a thickness of 2μm, as shown in Figure 5.8.

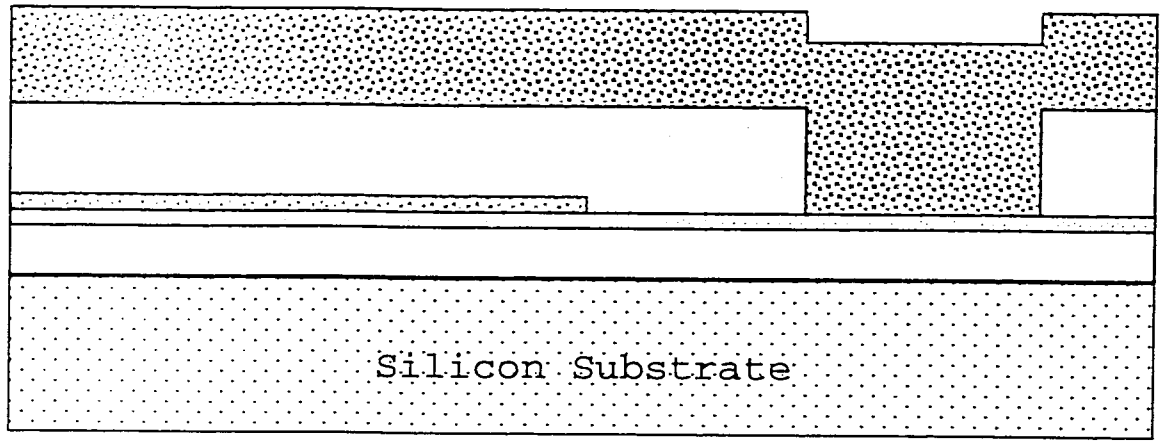

FIGURE 5.8 A 2μm polysilicon layer is deposited, and is anchored to the first polysilicon layer.

A thin oxide layer (500 nm) is deposited above the structural polysilicon and helps to achieve straight sidewalls when etching the thick structural polysilicon layer, and which also allows for thinner lithographical gaps, since it eliminates the need for a thick photoresist [14]. Photoresist is an organic polymer which is soluble in a special solvent unless it has been polymerized by

exposure to light. By selectively exposing the photoresist and then etching it in the solvent, patterns may be opened in the surface of the resist. The wafer is dipped in hydrofluoric acid, which etches away the sacrificial oxide layer and leaves all other layers intact. The released MEMS structure is as shown in Figure 5.9.

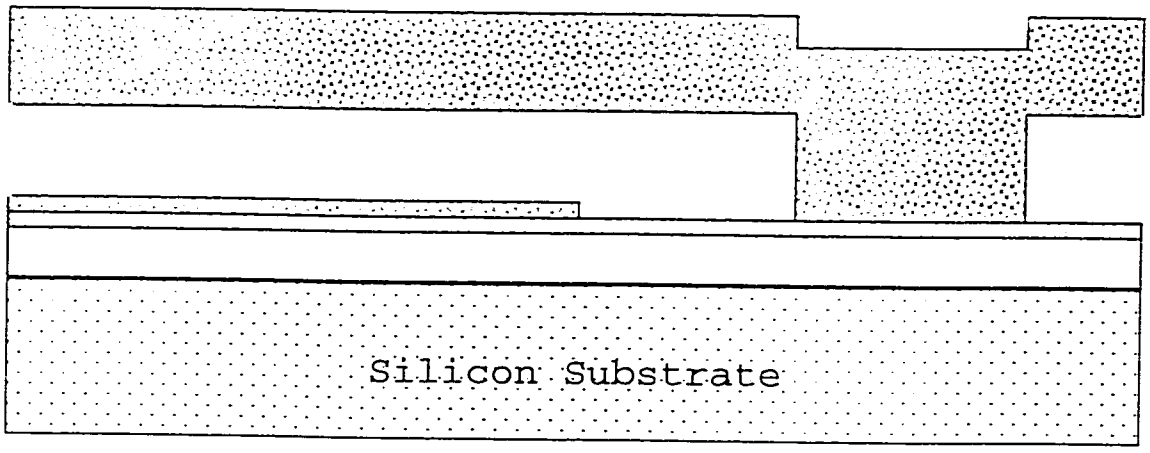

FIGURE 5.9 The sacrificial oxide layer is etched, leaving all other layers intact.

5.2 3-D FEA SIMULATION USING INTELLISUITE

The natural frequencies and corresponding mode shapes of both the individual resonators and the two-resonator filter are obtained through natural frequency analysis. IntelliSuite can compute the natural frequency shift of a structure due to the application of external electrostatic forces. This requires non-linear analysis assumptions. The applied force will have an effect on the non-linear stiffness of the system. From the modified stiffness matrix, IntelliSuite can solve the eigenvalue problem to obtain the natural frequencies. The full 3-D effect of these forces is taken into account. No macro-model or rigid body assumption is made. The analysis takes into account six degrees of freedom at every nodal point [31]. This allows us to investigate the programmability of the

MEMS filter. A discussion on the methods used and the sensitivity of the results follows. A mode based transient analysis is used to find the filter displacement response curve in the frequency domain (filter spectrum) from which the electrical gain can be obtained.

The computer used for all FEA simulations herein, has been a Sun Ultra 10 (Ultra SPARC – IIi) with a 333 MHz CPU and 256 MB RAM.

5.2.1 Resonator Design Using Existing Prototype

Wang and his coworkers at the University of Michigan [6] have designed a resonator with tuning fingers placed on the resonator shuttle (body of resonator), that allow changes of individual resonator center frequencies. It is possible that the displacement of the resonator, if at a high enough level, can cause non-linearities in the resonator spring. By instead placing the tuning fingers on the truss, it is possible to minimize such non-linearities, since they will be moving at only half the displacement of the shuttle.

The dimensions comparable to that of [6] were used in this design simulation with IntelliSuite. The resonator was designed with a beam length L = 70 μm, and width W = 2 μm resulting in K = 43.264 N/m. The equivalent mass of the resonator is M = $1.54X10^{-11}$ Kg, giving a center frequency of 267 kHz. Figure 5.10 shows the IntelliSuite layout of this resonator.

FIGURE 5.10 IntelliSuite layout of single-comb resonator.

A tuning range of 267 to 261.66 kHz was found for a 0-100 V range in tuning voltage. Note from Figure 5.10 that the parallel plate structures that allow voltage-controlled tuning of resonator center frequencies are placed on the truss instead of on the shuttle location.

5.2.2 Two-Resonator MEMS Filter Design

The frequency characteristic for the two-resonator MEMS filter (tested earlier using SPICE) is now predicted by 3-D finite element analysis (FEA) simulation using IntelliSuite. Given the filter specifications summarized in Tables 3.1 and 3.2, a set of masking steps were developed to fabricate both the single resonator and the coupled two-resonator programmable MEMS bandpass filter using the IntelliSuite Process Table.

The file from the Process Table is imported into the Electro Mechanical module so that the resonance modes of the structure can be examined. In the Electro Mechanical analysis window, the resonator anchors and fixed tuning fingers are fixed by selecting *Boundary* and *Fixed*. IntelliSuite has automatically meshed files that are imported from the Process Table. By selecting *Coarse*, we can view the number of nodes the mesh contains. Selecting *Coarse* will also initialize the Analysis menu. The mesh can be viewed by going to *View*, *Mesh*.

IntelliSuite uses 20-node parabolic brick elements because of the high quality and accuracy of these elements. After extensive numerical testing, linear elements (such as 8-node brick elements) were found to be inefficient for MEMS simulations. These linear elements usually require a prohibitively fine discretization (especially through the thickness) which leads to large numerical models [31].

Tests on the tetrahedral family of elements also showed that a larger number of nodes and elements are required to achieve the same accuracy as a mesh consisting of 20-node brick elements. In MEMS applications especially, the tetrahedral elements in a mesh comprised solely of tetrahedrons can become highly distorted leading to numerical inaccuracies [31].

The current mesh does not appear to be acceptable, as each of the beams is one brick element, so it is more finely discretized. Instead of refining the mesh in the entire structure, we refine the mesh only in the areas that play an important role in the mechanical analysis. In this case, the beams are refined by going to *Mesh*, *Mech_mesh*, and selecting each of the beams. A dialog box appears and a maximum mesh size must be entered. For example, a maximum mesh size of 3 μm is chosen for the length of the beams (creating 50 elements along the length of the beam). The beams are refined to 2 elements thick by 3 elements in width and segmented into 50 elements in length. The improvement obtained with these measurements over the less finely discretized mesh of 30

elements along the length of the beams and no refinement of thickness or width of the beams, is approximately 2-%. Finer mesh refinements add computation time and are not worth the improved accuracy in the results. With further discretization of the measurements, results remain quite similar, but computation time increases significantly, form approximately ½ hour to over 2 hours.

To visualize and update the mesh, the following commands are used: *Mesh*, *Selection Mode*, *Check & Update*; then *Mesh*, *Mech_mesh* and finally *View*, *Mesh*. Figures 5.11 and 5.12 show the refined mesh and a zoomed view of the refined mesh, respectively.

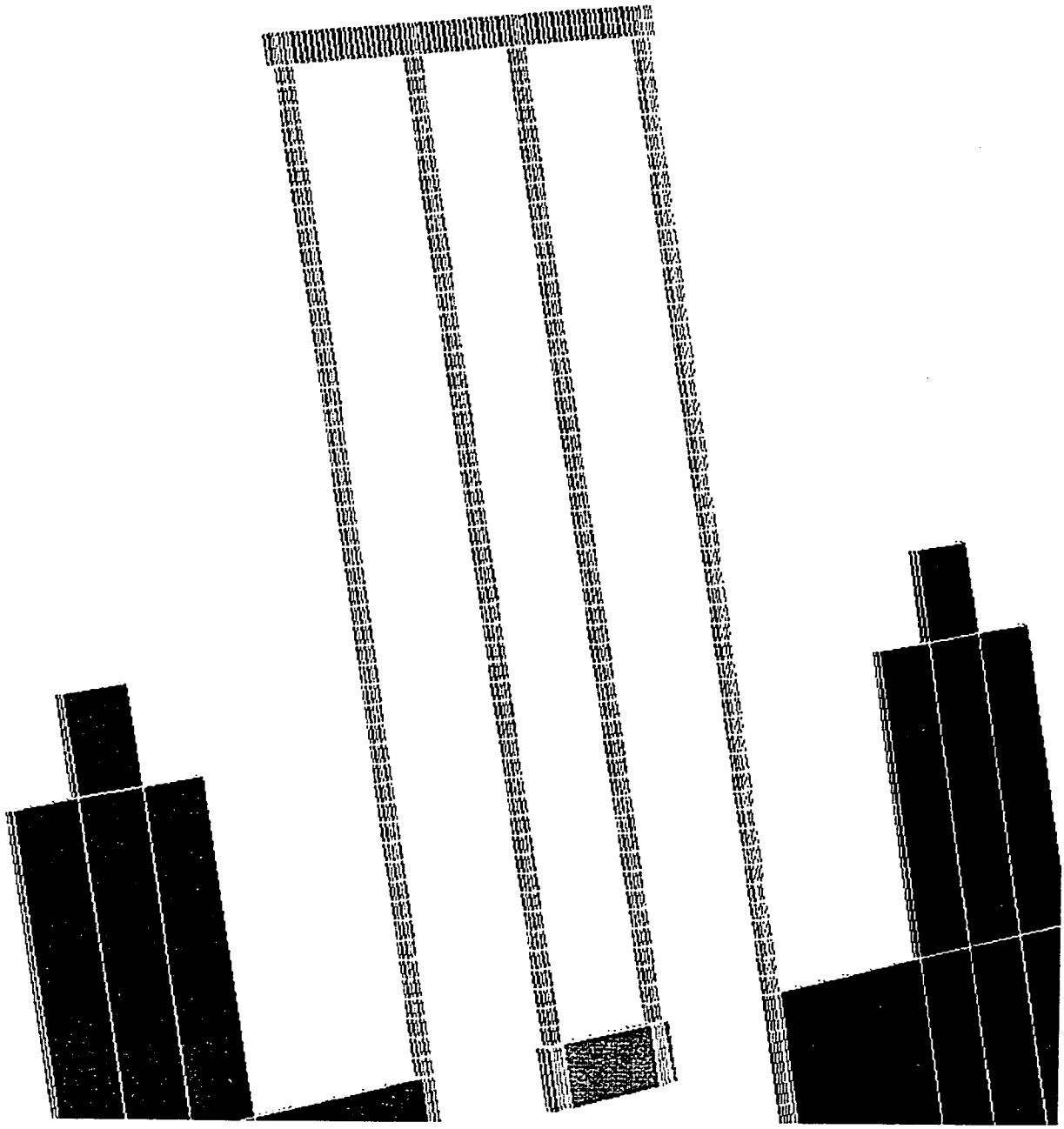

FIGURE 5.11 Mechanical mesh refinements to beams.

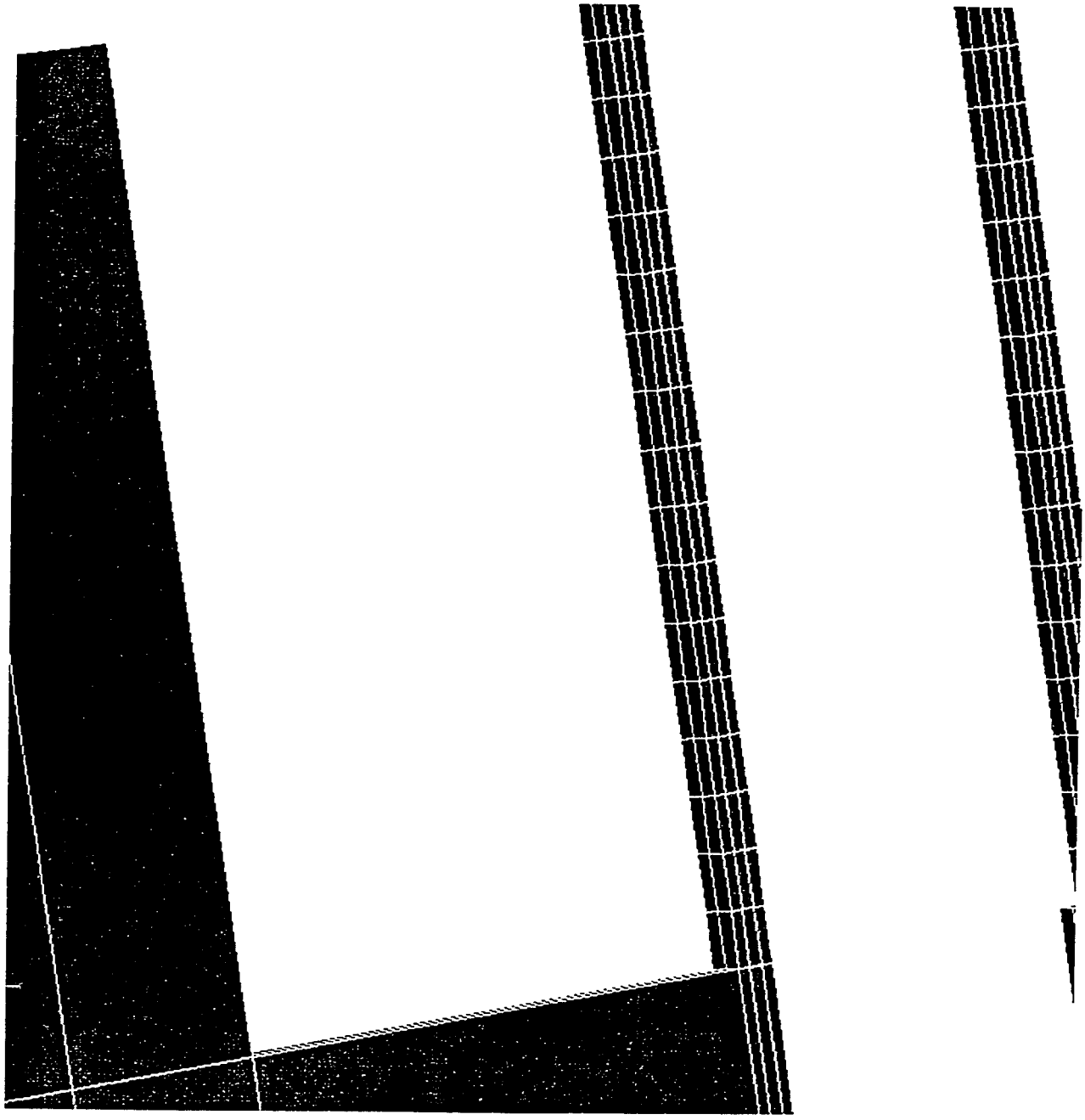

FIGURE 5.12 Mechanical mesh refinements to beams (zoomed in).

To simulate the frequency response of this MEMS filter we need to define the loading conditions. In the *Loads* pull-down menu, we choose *Amplitude vs. Frequency*, *Tabular*. The data points defining the loading in the frequency

domain are then entered. A voltage is applied to the filter input, or signal sending port (in Figure 2.1), that creates an electrostatic drive force proportional to the applied voltage V_i=10V (maximum voltage value of the AC waveform for our MEMS filter). This drive force is [1]

$$F = V_{Pi}\left(\frac{\partial C}{\partial x}\right)_i V_i \tag{5.1}$$

where V_{Pi} represents the DC bias at the input port, V_{pi}=10V. The magnitude of the input force is constant at F (Equation 5.1), while its frequency is swept through the frequency range we are investigating.

A quality factor must also be defined under *Analysis*, *Dynamic (Mode Based)*, *Mode Damping Definition* by giving a damping factor ξ_i for each of the vibrational modes specified. The relationship between the mass damping factor α and the stiffness damping factor β is [30]:

$$\xi_i = \frac{\alpha}{2\omega_i} + \frac{\beta\omega_i}{2} \tag{5.2}$$

where ω_i is the mode frequency. The associated quality factor Q can be expressed as [30]

$$Q = \frac{1}{2\xi_i} \tag{5.3}$$

A damping definition was calculated using Equation 5.3 assuming a quality factor Q=20; this value is found experimentally in [1].

Under *Analysis*, choosing *Dynamic (Mode Based)*, *Steady State Dynamics* brings up a frequency range dialog box in which the frequency range to investigate is defined along with the number of points between modes [30]. Figure 5.13 shows the frequency characteristic for a single stand-alone resonator as predicted by 3-D FEA simulation using IntelliSuite.

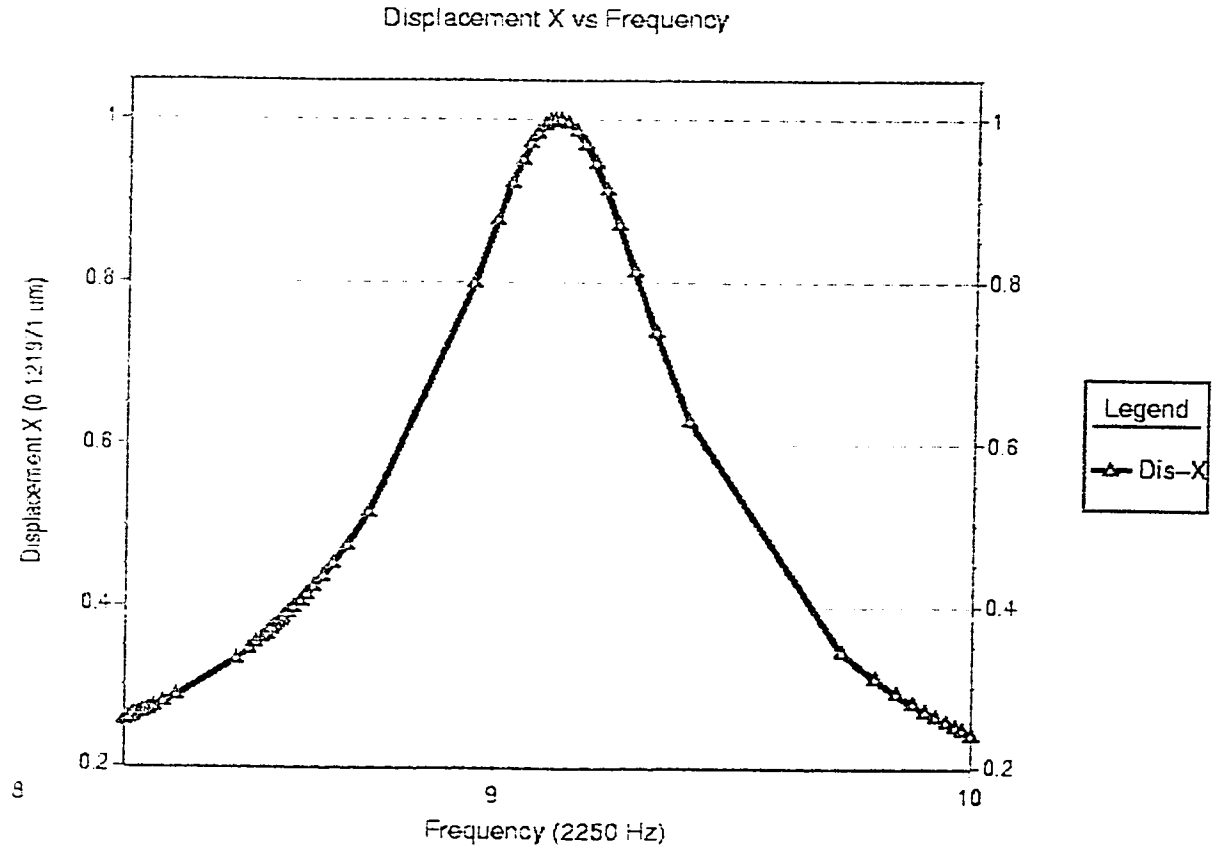

FIGURE 5.13 Frequency characteristic for the stand-alone comb-resonator using 3-D FEA simulation with IntelliSuite.

These MEMS filters process electronic signals, thus it is important to express the gain of the filter in terms of electrical variables. For our purposes this would be current out / voltage in. 3-D FEA simulations with IntelliSuite cannot calculate these variables directly so we will need to use analogies. Such a relation may be obtained by relating the internal mechanical parameters F and X to the corresponding electrical input and output through the phasor relations [1, 6, 14]

$$V_i = \frac{F}{V_{Pi}\left(\frac{\partial C}{\partial x}\right)_i} \tag{5.4}$$

$$I_o = V_{Po}\left(\frac{\partial C}{\partial x}\right)_o j\omega X \tag{5.4}$$

where V_{Pi} and V_{Po} represent the dc bias at the input (signal sending port) and output (signal sensing port), respectively, as shown in Figure 2.1. $\partial C/\partial x$ is the capacitive change with respect to comb motion at the respective ports and can be approximated by Equation 2.13. Hence, the filter transconductance can be expressed as

$$\frac{I_o}{V_i} = j\omega V_{Pi} V_{Po}\left(\frac{\partial C}{\partial x}\right)_i\left(\frac{\partial C}{\partial x}\right)_o \frac{X}{F} \tag{5.5}$$

and the electrical gain as

$$\left|\frac{I_o}{V_i}\right| = \omega V_{Pi} V_{Po}\left(\frac{\partial C}{\partial x}\right)_i\left(\frac{\partial C}{\partial x}\right)_o \frac{X}{F} \tag{5.6}$$

where the displacement X is approximated off the IntelliSuite graph (since there is no way to export the data directly from IntelliSuite) for a given frequency. Figure 5.14 shows this conversion into electrical parameters for the single resonator frequency response.

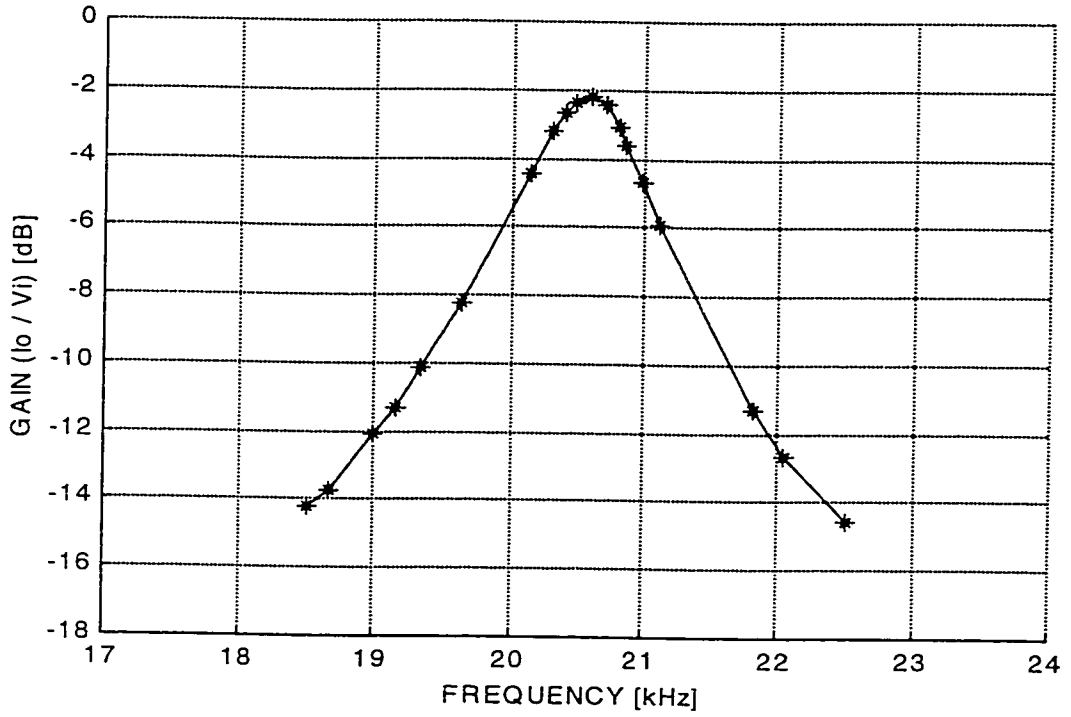

FIGURE 5.14 Frequency characteristic for the stand-alone comb-resonator using 3-D FEA simulation with IntelliSuite and converting this gain into electrical parameters.

The graph (Figure 5.14) is very similar to the graph obtained by SPICE (Figure 3.7), showing good prediction by ODEs. We have yet to examine the programmability of the filter.

Elec_mesh is used to activate the Exposed Face Mesh algorithm (EFM), for the 3-D coupled electromechanical analysis. When compared to the commonly used volume refining mesh method, the EFM algorithm shows substantial improvement in increasing accuracy of results and reducing computational time and memory expenses [31]. Instead of refining the volume mesh, *Elec_mesh* can be used to refine only the electrostatic surface mesh on chosen Exposed Faces. The advantage of this method is that the surface mesh used in the electrostatic analysis is separated form the mechanical volume mesh while assuring full compatibility between the two [31].

When designing the MEMS bandpass filter, the accurate calculation of electrostatic pressure on the structure surface is essential in determining the structural deformation and natural frequencies [31]. The movable finger faces on which the electrostatic pressure is critical for determining the electromechanical behavior of the MEMS bandpass filter must be more finely refined. Zooming in on the Exposed Faces where the electrostatic mesh refinement will occur and going to *Mesh*, *Elec_mesh*, and choosing the Exposed Faces will bring up a dialog box. Selecting a refinement factor of 4 actually refines the mesh $2N^2$ or 32 times. To view and update the electrical mesh the following commands are executed: *Mesh*, *Selection Mode*, *Check Only*; then go to *Mesh*, *Elec_mesh*. Figure 5.15 shows a close-up view of the electrostatic mesh refinements on the tuning fingers. Simplifications can be made for the faces that play a minimal role in the electrostatic analysis, since these faces do not need to be refined. Even if these are removed completely from the analysis (by selecting them and setting N=0), the natural frequency results will remain sufficiently accurate for our purposes. This simplification can be made to the top face of the movable finger and the surface parallel to the substrate that are visible on the entity of Figure 5.15. The modes of vibration we are interested in are perpendicular to these electrostatic forces. Thus, the electrical loading will have little to no effect on the frequencies of these modes [33].

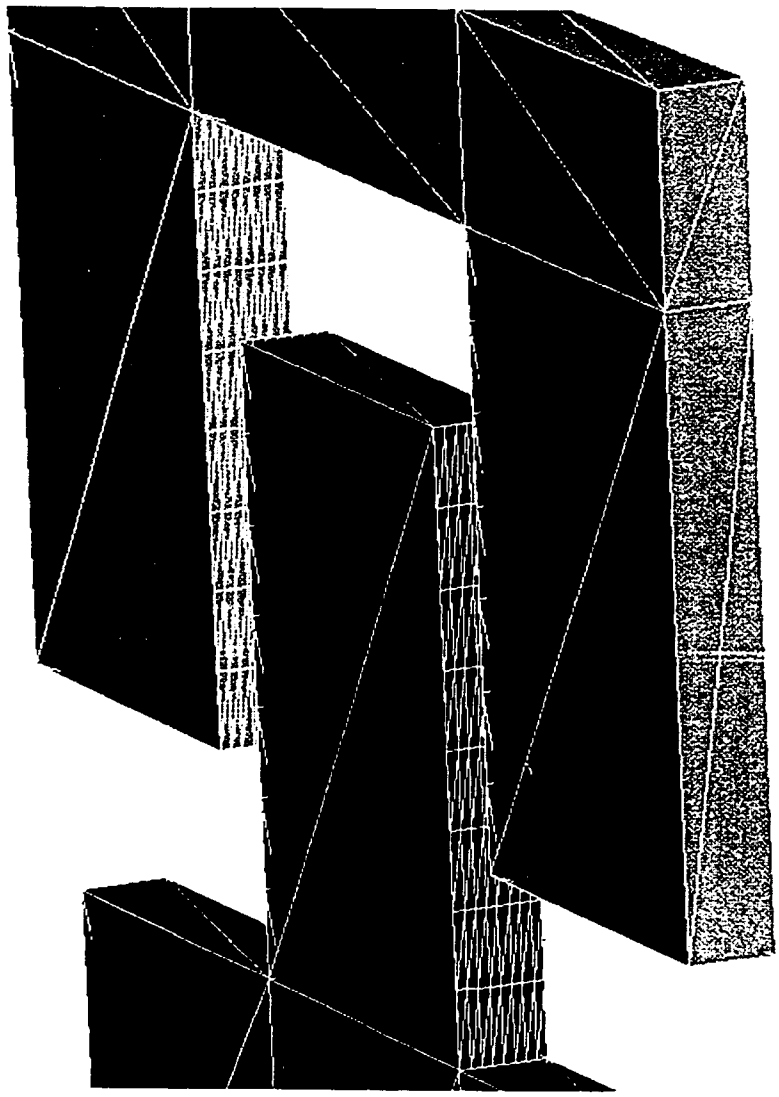

FIGURE 5.15 Close-up view of the electrostatic mesh refinements on tuning fingers.

The default electrostatic mesh was gradually refined in the areas of high electrostatic pressure until consistency in the accuracy of the results was obtained. Figure 5.16 shows a graph of the lateral-directed vibrational mode natural frequency for a DC bias voltage difference of 12 V (V_{tr} = 12 V DC) between the fixed and movable fingers as the value of N is increased.

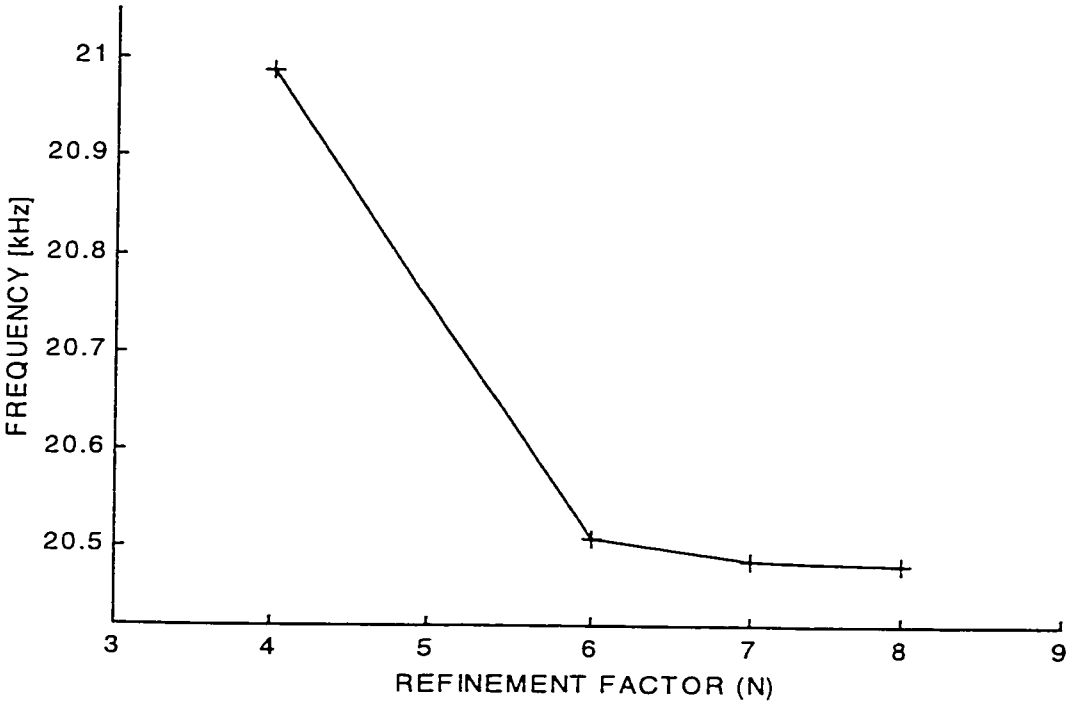

FIGURE 5.16 Vibrational frequency of single resonator (for a tuning voltage V_{tr} = 12 V DC) versus increasing N.

An excellent example of convergence of the center frequency is shown in Figure 5.16. In order to obtain the vibrational frequencies for higher voltage bias values a larger electrostatic mesh refinement factor is necessary.

Figure 5.17 shows the theoretical and simulated plots of resonance frequency versus tuning voltage for the single-comb resonator. The change in center frequency of one of the filter's resonators would also occur in the case of the two resonator filter. In the interest of computation time, we will use the single filter's resonator in the following analysis.

The practical tuning range is lower than predicted by Equations 2.21 – 2.23. A 5-% change in the filter's center frequency is observed for a voltage V_{tr} = 18 V DC. There are discrepancies between the lumped parameter model (line) and the 3-D FEA results (triangles). The lumped parameter equations predict the

frequency variations well until about 15 volts DC, however they are inadequate to accurately predict the programmability of the filter beyond this range.

The degree of programmability is a function of beam frequency and resonator stiffness. Assuming that the thickness dimension h is fixed by technological considerations, frequency increases are most conveniently achieved by shortening the beam length L [5]. The reason for this is that larger values of stiffness show a much slower change in frequency values as the applied voltage increases since the effective stiffness decreases with the square of the applied voltage. Moreover, a larger change in resonant frequency is observed for a resonator having a smaller mass since the change in frequency is much more sensitive to variations of stiffness (Equation 2.22).

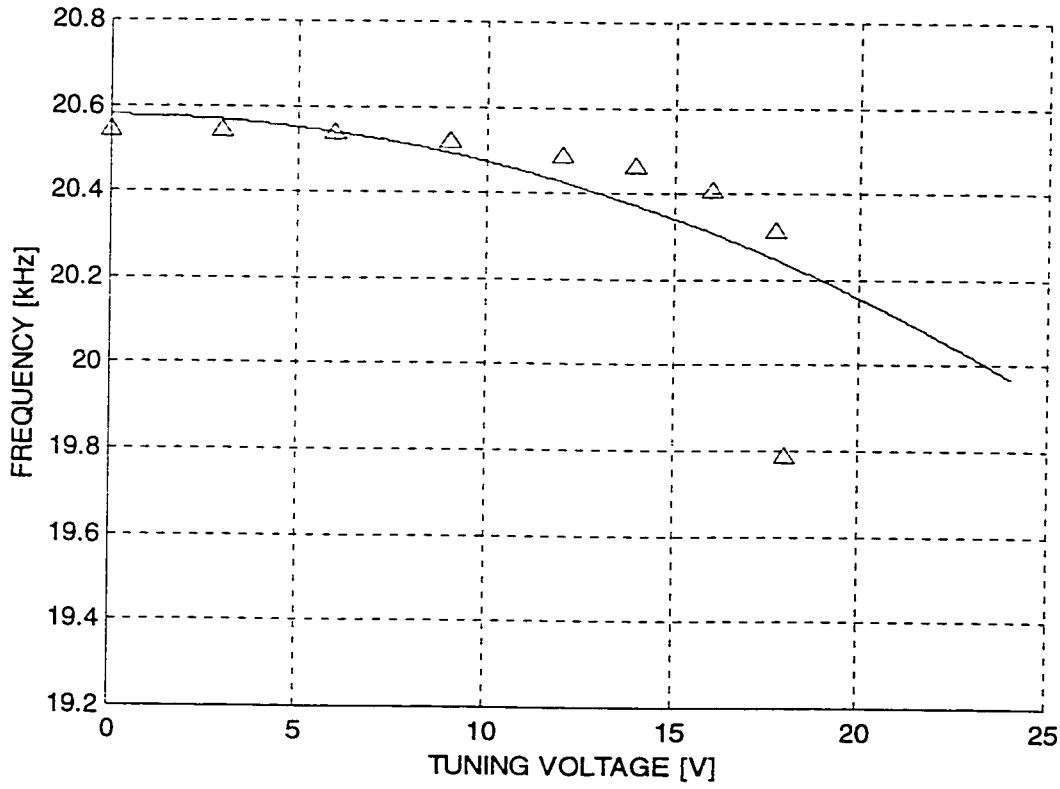

FIGURE 5.17 Theoretical and simulated plots of resonance frequency versus tuning voltage for the single-comb resonator.

The two-resonator programmable MEMS filter is simulated by a 3-D FEA simulation with IntelliSuite. The refinements of the mechanical mesh for the beams are carried out in order to assure the accuracy of the results. This is also true in the case of the electrostatic surface mesh for areas of high electrostatic pressure.

Figure 5.18 shows the frequency characteristic for the two-resonator MEMS filter as predicted by 3-D FEA simulation using IntelliSuite. A force was applied to the input of the first resonator equivalent to an electrostatic drive force of V_i=10V applied to the input port and the DC bias at the input port V_{pi}=10V. The quality factor Q=20 was assumed for the simulation (same loading and damping definitions as the single resonator case).

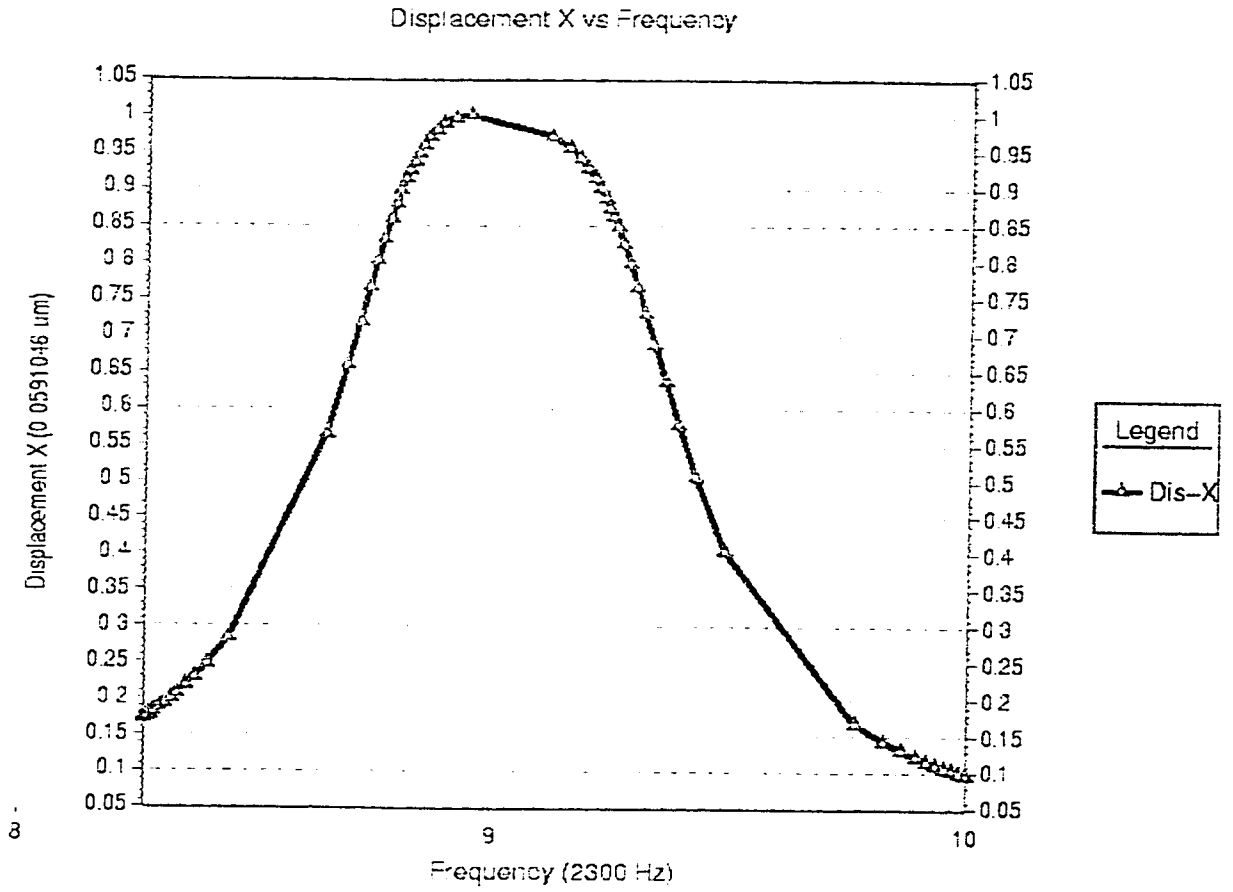

FIGURE 5.18 Frequency characteristic of the two resonator coupled filter using 3-D FEA simulation with IntelliSuite.

Figure 5.19 shows the gain of Figure 5.18 expressed in electrical parameters.

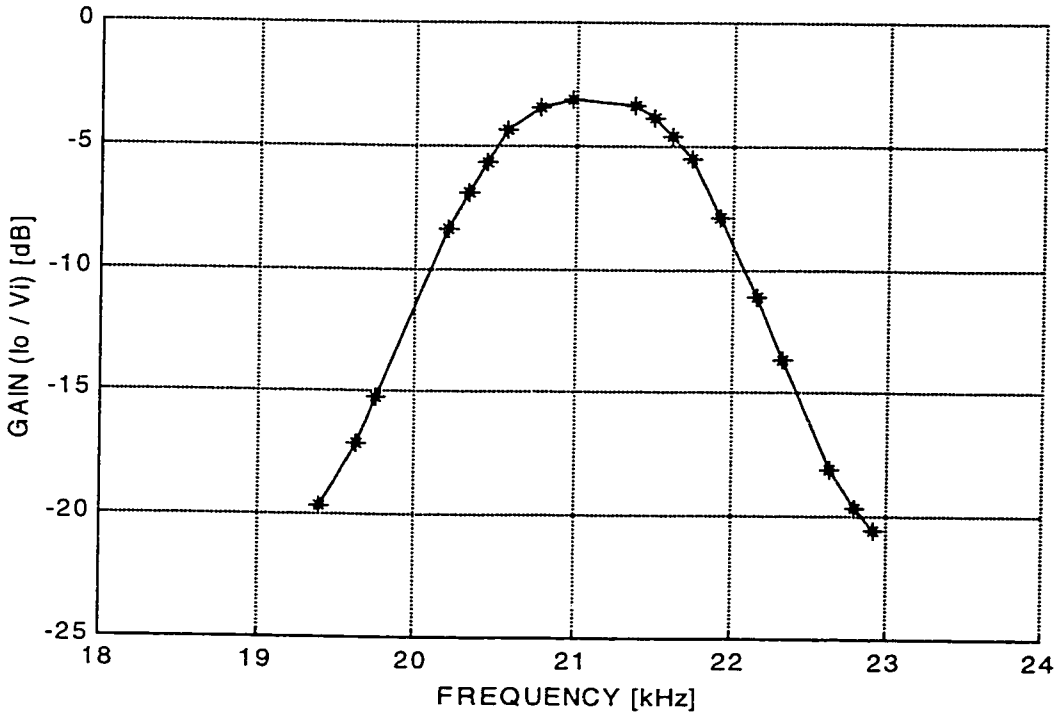

FIGURE 5.19 Frequency characteristic of the two resonator coupled filter using 3-D FEA simulation with IntelliSuite expressed in electrical parameters.

Figure 5.20 shows the effect of increasing the spring's bias voltage on the difference between the two frequency modes (f_2 - f_1). The relative spacing between these two mode peaks directly affects the bandwidth of the filter. The bandwidth of the filter increases as the difference between the two modes becomes larger.

At about 12 Volts, the difference between the two frequency modes has increase by 400 Hz. Frequency mode f_2 does not change because the center of the spring is motionless in this mode of vibration.

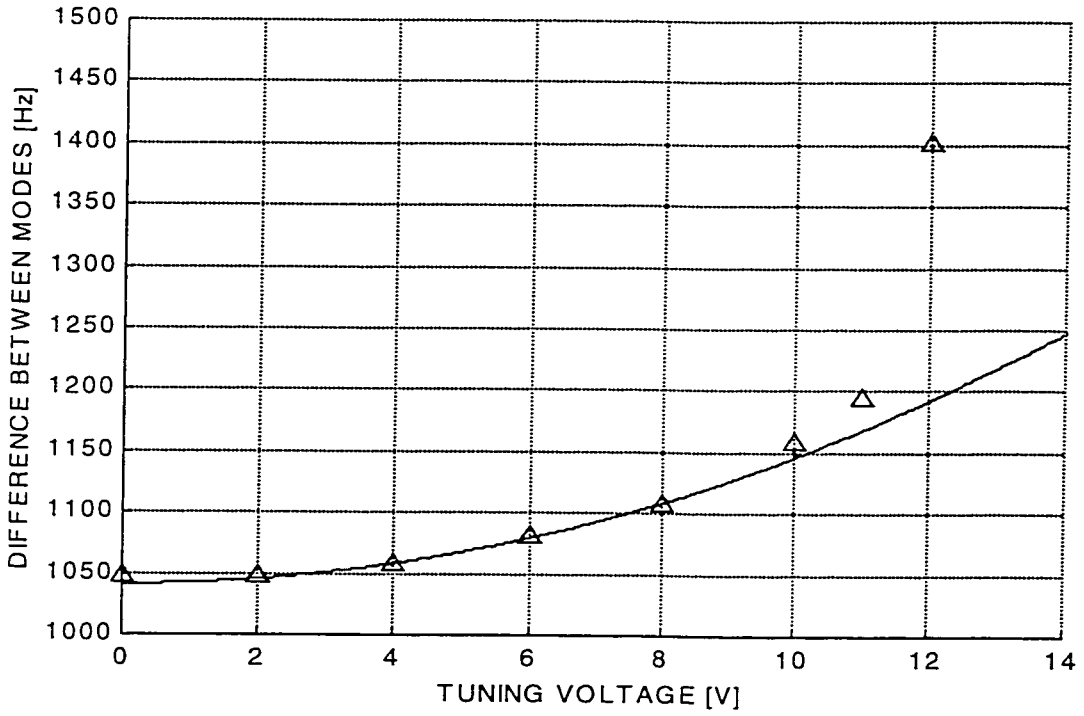

FIGURE 5.20 Simulated plot of the difference between the two resonance modes of the two resonator programmable MEMS filter.

The goal of obtaining some of the most differentiated results possible has been accomplished using V_{tr} = 18 V DC and V_{ts} = 12 V DC.

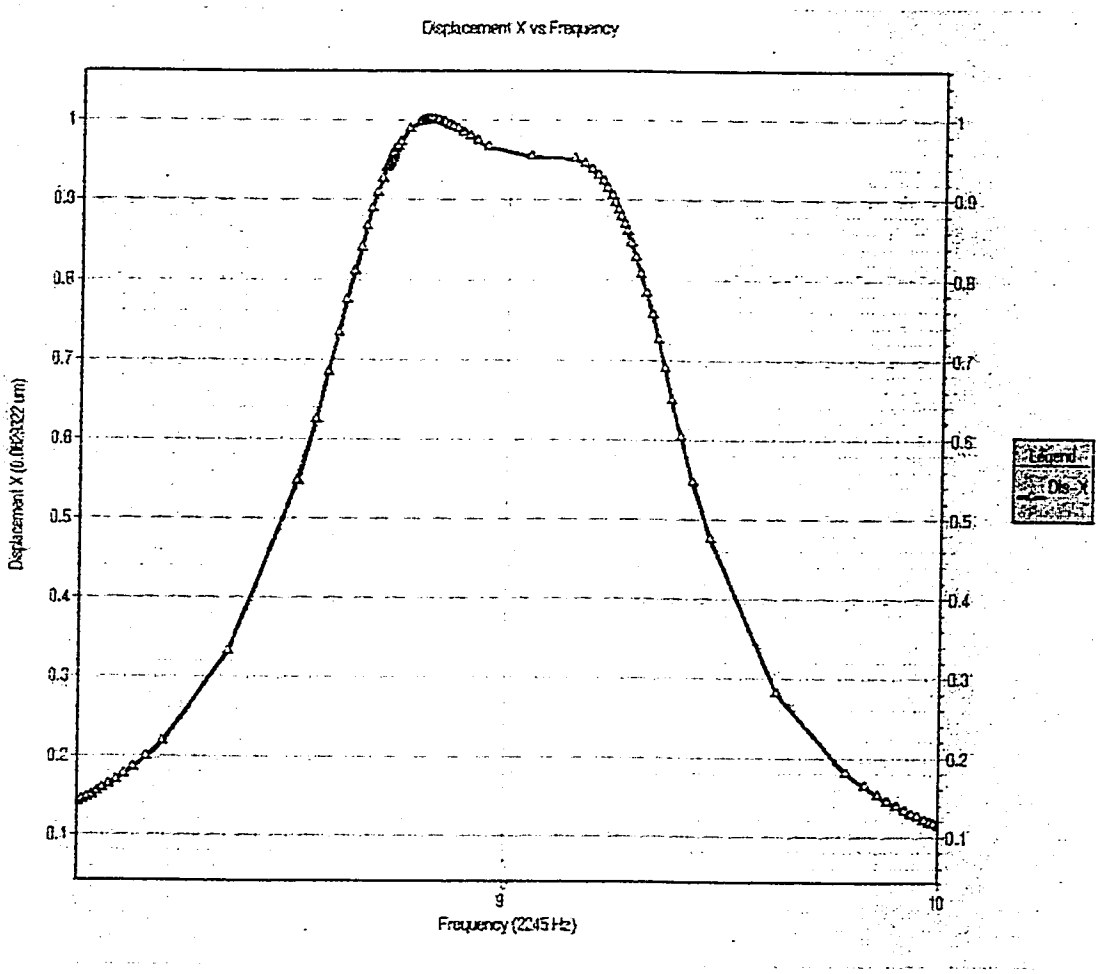

FIGURE 5.21 Frequency characteristic of the two resonator coupled filter using 3-D FEA simulation with IntelliSuite with V_{tr} = 18 V DC and V_{ts} = 12 V DC.

Figure 5.22 shows the above graph in electrical parameters (on the left) with Figure 5.19 superimposed (on the right).

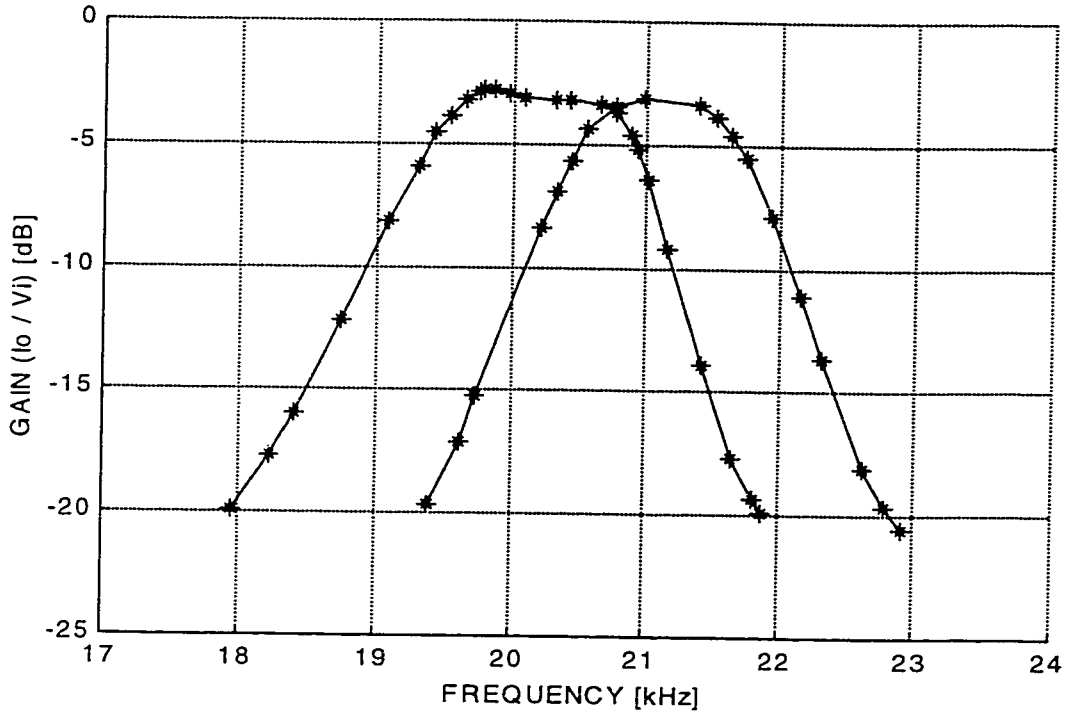

FIGURE 5.22 Frequency characteristic of the two resonator coupled filter using 3-D FEA simulation with IntelliSuite with V_{tr} = 18 V DC and V_{ts} = 12 V DC (on the left) and Figure 5.19 superimposed (on the right).

The nominal filter frequency (no voltage biases) depicted in Figure 5.22 (left), has a center frequency of 21.1 kHz and a 3-dB bandwidth of 1.2 kHz. The frequency characteristic of the filter in Figure 5.22 (right), with biases, has a center frequency of 20.1 kHz and a 3-dB bandwidth of 1.55 kHz.

The change in center frequency (Δf) and the change in 3-dB bandwidth (ΔBW_{3dB}) can be defined as

$$\Delta f = \frac{f_r - f_0}{f_0} \times 100\% \tag{5.7}$$

and

$$\Delta BW_{3dB} = \frac{BW_{3dB} - BW_{3dB0}}{BW_{3dB0}} \times 100\% \tag{5.8}$$

where the subscript 0 depicts the nominal filter parameter, which is subtracted from the extreme programmable range. The percentage change in center frequencies between no bias and with bias amount to 4.74 %, with a 29.17 % change in 3-dB bandwidth.

The reason for using only these two extreme cases in the comparison analysis is due to the extremely long computation time needed to obtain results, which can be over 48 hours in length.

5.3 DISCUSSION

Chapter 5 begins with detailed fabrication steps for the MEMS bandpass filter of this work. The filter is imported into IntelliSuite's Electro Mechanical module for analysis. Mesh refinements are performed to the default mechanical and electrostatic grids. A very accurate solution was obtained by generating this refined finite element model. The filter's nominal frequency response was obtained through a mode based transient analysis. The natural frequency shift due to the application of electrostatic forces was computed through a natural frequency analysis.

There are discrepancies between the lumped parameter model and the FEA results. There is a close correlation between ODE results and FEA simulations up until a certain range of the filter's programmability. After this range the 3-D FEA results drop off sharply. These discrepancies arise due to the simplistic lumped parameter model being inadequate to consider the distributed 3-D geometry of the microstructure. The theoretical lumped parameter approximations (ODEs) indicate a simplified one-dimensional model. The distributed FEA model is necessary to predict the filter's frequency programmability. Using ODEs, the filter programmable range rather large.

However, through FEA, the two-resonator programmable MEMS bandpass filter showed a programmability of 4.74 % in center frequency and 29.17 % in 3-dB bandwidth. More generous numbers cannot be obtained (with any accuracy) as electrostatic mesh refinements show a great variance in frequency results. These values represent the limits of programmability for this particular filter as predicted by 3-D FEA simulations.

6

CONCLUSION

A programmable bandpass filter based upon the use of polycrystalline silicon microelectromechanical (MEMS) resonators have been designed and simulated. Programmability was achieved by using parallel-plate structures to generate electrostatic forces that alter the frequency response of the MEMS implementation of the filter. The two-resonator programmable MEMS bandpass filter showed a programmability of 4.74 % in center frequency and 29.17 % in 3-dB bandwidth.

In order to maximize the programmability range of the filter, it is necessary that the following two conditions be satisfied: (1) The equivalent stiffness, both resonators and coupling spring, must be increased, and (2) The mass of the individual resonators and coupling spring be decreased. This variation of the parameters associated with the mass and spring constants has been shown to have the greatest effect on the range of programmability. It should suffice to say that the programmability ranges reported above represent the extent of this filter's programmability.

Through theoretical analysis, the resonant frequency modes of a MEMS filter can be expected to vary with tuning voltage, resulting in a change of the filter passband. These relationships were substantiated by 3-D FEA simulation

with IntelliSuite MEMS design and simulation software. A comparison of values computed using lumped parameter methods (ODEs) and distributed parameter methods (3-D FEA) has been carried out.

Calculations by 3-D FEA simulation show that the resonant frequencies vary approximately parabolically with voltage, as predicted by theory. The theoretical (ODE) model predicted a relatively linear variation of the center frequency with applied voltage while the 3-D FEA analysis showed that there was a discontinuity in a certain frequency range.

3-D FEA simulation results are necessary to accurately predict the frequency variation properties of the programmable MEMS filter. While theoretical lumped parameter approximations (ODEs) indicate a simplified estimate of the actual physical properties.

The results obtained with a finite element analysis depend on the geometry and size of the finite elements together with numerical method considerations. Nevertheless, a very accurate solution has been obtained by generating a proper finite element model, through mesh refinements.

The theoretical ODE equations used for this filter simplify its motion in only one direction. Thus, these models do not accurately describe the programmable MEMS bandpass filter demonstrated in this work. In general, 3-D structures have more than one degree-of-freedom. FEA models the 3-D distributed system more accurately and this is the reason FEA gives much more accurate results than a simple lumped parameter approximation based on the use of ODEs.

The FEA method is very computationally intensive and a calculation time of 48 hours was not uncommon on a SPARC Ultra 10 workstation for a transient mode based FEA.

The programmable strategies demonstrated for a two-resonator MEMS bandpass filter can greatly alleviate the nonideal effects of microelectromechanical filters as well as provide a programmable filter capability, in both the filter's center frequency and bandwidth, which is key to successful microscale mechanical filter implementation. These design strategies will most likely become increasingly important as the frequency and order of microelectromechancial filters rise to accommodate the needs of specialized signal processing and communications operations.

6.1 FUTURE WORK

The proposed filter geometry demonstrated herein has important implications for future designs of programmable micromechanical electronic filters. By further exploiting the flexibility of the "electrostatic spring", resilient frequency programmable architectures can be envisioned.

A MEMS based filterbank architecture could be designed and implemented that would allow for a high degree of programmability associated with center frequency and bandwidth.

As far as reproducibility and predictability of MEMS filters is concerned, much work still has to be done. However, as these filters are reduced in size to achieve higher frequency ranges, perhaps with the introduction of NEMS (Nano-Electro-Mechanical-Systems), improvements in the programmability (both in percentage and range) of these 3-D filters will become more significant.

The packaging of MEMS filter implementations has not been considered in depth in this thesis and lends itself to continuing research in the future.

Appendix A

RESONANCE FREQUENCY OF MEMS RESONATORS [6]

To aid in the derivation of the effective mass and stiffness of a micromechanical resonator, Figure A.1 presents the shape of a micromechanical resonator with shuttle displaced by a distance X_s under an applied force F_x in the *x* direction. Other relevant dimensions and variables are also included in the figure.

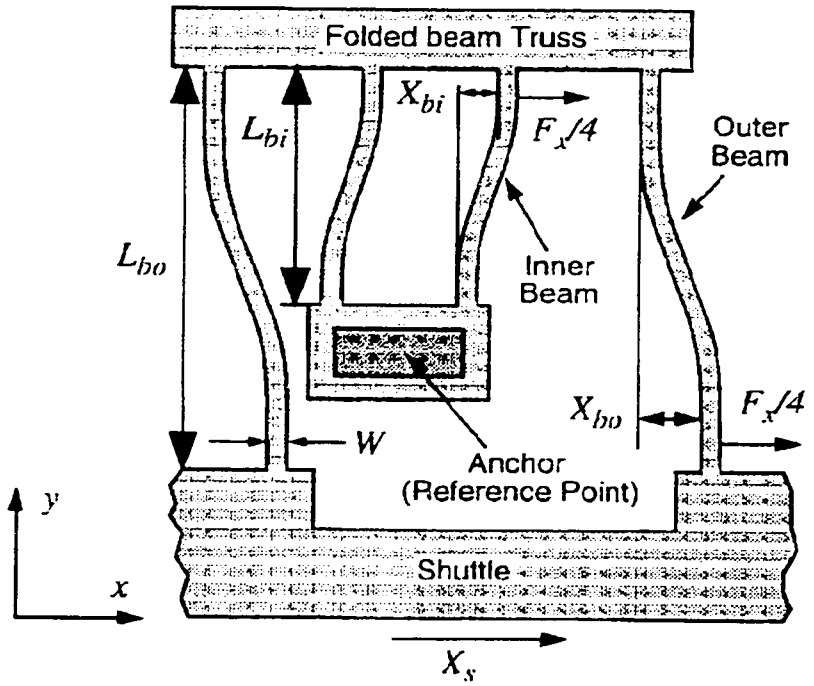

FIGURE A.1 Schematic presenting the shape of a micromechanical resonator with shuttle displaced by a distance X_s under an applied force F_x in the *x* direction.

The resonant frequency of a microresonator can be approximated using Rayleigh's principle

$$KE_{\max} = PE_{\max} \tag{A.1}$$

where KE_{max} and PE_{max} are the peak kinetic and potential energies achieved over a vibration cycle. Using Figure A.1

$$KE_{\max} = KE_s + KE_{bi} + KE_{bo} + KE_t = \frac{1}{2}\left[v_s^2 M_s + v_t^2 M_t + \int v_{bi}^2 dM_{bi} + \int v_{bo}^2 dM_{bo}\right] \tag{A.2}$$

where the M's represent the masses, and the v's represent peak velocities, with subscripts s, bi, bo, and t corresponding to the shuttle, the inner and outer beams and the trusses, respectively. With a peak velocity of $\omega_0 X_s$, the peak kinetic energy for the shuttle can be written directly as

$$KE_s = \frac{1}{2}(\omega_0 X_s)^2 M_s \tag{A.3}$$

To determine the peak kinetic energies of the inner and outer beams, the peak velocity as a function of location y must be determined for each. By considering stiffness relationships, these velocities can also be written in terms of the shuttle displacement X_s. Under fixed-fixed sliding boundary conditions, the stiffness of a flexural beam is given by

$$k = \frac{12EI}{L^3} \tag{A.4}$$

where k is the stiffness of the beam, E is the Young's modulus of its material, I is the bending moment of inertia of the beam and is given by

$$I = \frac{hW^3}{12} \tag{A.5}$$

and h, W and L are its thickness, width, and length, respectively. Using Equation A.4, and with reference to Figure A.1, the stiffness of the inner and outer beams are related by

$$\frac{k_{bo}}{k_{bi}} = \left(\frac{L_{bi}}{L_{bo}}\right)^3 \tag{A.6}$$

Given that force in the spring system is divided evenly between each inner-outer beam pair, and the inner and outer beams of a given pair each see the same force equal to $F_x/4$, this stiffness ration can also be written in terms of peak beam deflections

$$\frac{k_{bo}}{k_{bi}} = \frac{X_{bi}}{X_{bo}} \tag{A.7}$$

Combining Equation A.6 and Equation A.7

$$\frac{X_{bi}}{X_{bo}} = \left(\frac{L_{bi}}{L_{bo}}\right)^3 = \frac{1}{\beta^3} \tag{A.8}$$

where β is the ratio of the outer beam length L_{bo} to the inner beam length L_{bi}. With reference to Figure A.1

$$X_{bi} = \frac{X_x}{1+\beta^3} \tag{A.9}$$

and the peak deflection profiles of the inner and outer beams as a function of y can now be expressed as

$$x_{bi}(y) = \frac{X_s}{1+\beta^3}\left[3\left(\frac{y}{L_{bi}}\right)^2 - 2\left(\frac{y}{L_{bi}}\right)^3\right] \tag{A.10}$$

$$x_{bo}(y) = X_s\left\{1 - \frac{\beta^3}{1+\beta^3}\left[3\left(\frac{y}{L_{bo}}\right)^2 - 2\left(\frac{y}{L_{bo}}\right)^3\right]\right\} \tag{A.11}$$

from which the respective peak kinetic energies (for all the inner beams and all the outer beams, respectively) can be written as

$$KE_{bi} = \frac{1}{2}\int_0^{L_{bi}} [\omega_0 x_{bi}(y)]^2 \frac{M_{bi}}{L_{bi}} dy \tag{A.12}$$

$$KE_{bo} = \frac{1}{2}\int_0^{L_{bo}} [\omega_0 x_{bo}(y)]^2 \frac{M_{bo}}{L_{bo}} dy \tag{A.13}$$

Recognizing a truss velocity equal to $\omega_0 X_{bi}$, and performing the needed integrations, the peak kinetic energy of the total system is found to be

$$KE_{\max} = \frac{1}{2}(\omega_0 X_s)^2 \left\{ M_s + \frac{M_t}{(1+\beta^3)^2} + \frac{13}{35(1+\beta^3)^2} M_{bi} + \left[\frac{1}{(1+\beta^3)} + \frac{13\beta^6}{35(1+\beta^3)^2} \right] M_{bo} \right\} \tag{A.14}$$

from which the effective mass at the shuttle can easily be identified as

$$m_{rs} = M_s + \frac{M_t}{(1+\beta^3)^2} + \frac{13}{35(1+\beta^3)^2} M_{bi} + \left[\frac{1}{(1+\beta^3)} + \frac{13\beta^6}{35(1+\beta^3)^2} \right] M_{bo} \tag{A.15}$$

To find the peak potential energy of the system, an expression for the stiffness seen at the shuttle location is required. For this purpose, the deflection profile of the inner beam can be rewritten in terms of the applied force $F_x/4$ to yield

$$x_{bi}(y) = \frac{F_x}{48EI}\left(3L_{bi}y^2 - 2y^3\right) \tag{A.16}$$

Evaluation Equation A.10 and Equation A.16 at $y=L_{bi}$, then equation them and solving, the stiffness at the shuttle location k_{rs} is found to be

$$k_{rs} = \frac{F_x}{X_s} = \frac{4Eh}{1+\beta^3}\left(\frac{W}{L_{bi}}\right)^3 \tag{A.17}$$

from which the peak potential energy in the system follows as

$$PE_{\max} = \frac{1}{2} k_{rs} X_s^2 = \frac{2EhX_s^2}{1+\beta^3} \left(\frac{W}{L_{bi}} \right)^3 \tag{A.18}$$

Using Equation A.14 and Equation A.18 in Equation A.1, the resonance frequency of this microresonator is found to be

$$\omega_0 = \sqrt{\frac{k_{rs}}{m_{rs}}} = \sqrt{\frac{4Eh(W/L_{bi})^3}{(1+\beta^3)m_{rs}}} \tag{A.19}$$

Appendix B

INTELLISUITE PROCESS OUTLINE

The following comprises a step-by-step outline of the IntelliSuite process.

```
Number of steps in Process: 20
1. Definition Si Czochralski 100
       Operation on both sides.
           t_film: 100000 nm
         diameter: 51201.6 mm
         flat_dir: 110 Vector
        dope_conc: 1e+15 /cm3
           resist: 2.54 Ohm-cm

2. Etch Si Clean Pirahna
       Operation on both sides.
       H2SO4_conc:  75 %
        H2O2_conc:  25 %
        time_etch:  10 min

3. Deposition SiO2 Thermal Wet
       Operation on both sides.
            T_dep: 1100 deg_C
            P_dep: 101325 Pa
        time_dep: 600 min
           H2Opp:  10 part.pr
Results:
          t_film: 500 nm
          t_etch: 500 nm
         t_after:   0 nm

4. Deposition Si3N4 PECVD Ar
       Operation on top side.
            T_dep: 275 deg_C
            P_dep: 127 Pa
          Rf_Pow: 250 W
         Rf_Freq: 13.56 MHz
          tot_fl: 1500 sccm
            Arpp: 0.959 part.pr
```

```
            NH3pp: 0.024 part.pr
           SiH4pp: 0.017 part.pr
Results:
           t_film: 100 nm

5. Etch Si Clean RCA
      Operation on both sides.
       time_etch:  30 min
          T_etch:  80 deg_C

6. Deposition PolySi LPCVD SiH4
      Operation on both sides.
            T_dep: 630 deg_C
            P_dep:  53 Pa
         time_dep:  15 min
           T_anne: 1100 deg_C
         time_an:   0 min
Results:
           t_film: 300 nm

7. Deposition PR-S1800 Spin S1805
      Operation on top side.
            Speed: 4000 rpm
        time_spin:  30 sec
           T_soft: 115 deg_C
        time_soft:  60 sec
           lambda: 436 nm
Results:
           t_film: 500 nm

8. Definition UV Contact Suss
      Operation on top side.
          mask_no: 901 #
            Power: 250 W
           lambda: 436 nm
         time_exp:  10 sec
Results:
             dose:  52 J

9. Etch PR-S1800 Wet 1112A
      Operation on both sides.
           T_etch:  20 deg_C
       time_etch:   5 min
Results:
           t_etch: 1e+06 nm

10. Etch PolySi Dry SF6-Plasma
      Operation on both sides.
       time_etch:  15 min
          P_base: 0.0001 Pa
Results:
           t_etch: 1e+06 nm

11. Etch PR-S1800 Wet 1165
      Operation on both sides.
           T_etch:  20 deg_C
       time_etch:   5 min
```

```
Results:
          t_etch: 1e+06 nm

12. Deposition PR-S1800 Spin S1805
      Operation on top side.
           Speed: 4000 rpm
       time_spin:  30 sec
          T_soft: 115 deg_C
       time_soft:  60 sec
          lambda: 436 nm
Results:
          t_film: 2000 nm

13. Definition UV Contact Suss
      Operation on top side.
         mask_no: 902 #
           Power: 250 W
          lambda: 436 nm
        time_exp:  10 sec
Results:
            dose:  52 J

14. Etch PR-S1800 Wet 1112A
      Operation on both sides.
          T_etch:  20 deg_C
       time_etch:   5 min
Results:
          t_etch: 1e+06 nm

15. Deposition PolySi LPCVD SiH4
      Operation on both sides.
           T_dep: 630 deg_C
           P_dep:  53 Pa
         time_dep:  15 min
          T_anne: 1100 deg_C
        time_an:   0 min
Results:
          t_film: 2000 nm

16. Deposition PR-S1800 Spin S1805
      Operation on top side.
           Speed: 4000 rpm
       time_spin:  30 sec
          T_soft: 115 deg_C
       time_soft:  60 sec
          lambda: 436 nm
Results:
          t_film: 500 nm

17. Definition UV Contact Suss
      Operation on top side.
         mask_no: 903 #
           Power: 250 W
          lambda: 436 nm
        time_exp:  10 sec
Results:
            dose:  52 J
```

```
18. Etch PR-S1800 Wet 1112A
      Operation on both sides.
          T_etch:  20 deg_C
       time_etch:   5 min
Results:
          t_etch: 1e+06 nm

19. Etch PolySi Dry SF6-Plasma
      Operation on both sides.
       time_etch:  15 min
          P_base: 0.0001 Pa
Results:
          t_etch: 1e+06 nm

20. Etch PR-S1800 Wet 1165
      Operation on both sides.
          T_etch:  20 deg_C
       time_etch:  50 min
Results:
          t_etch: 1e+06 nm
```

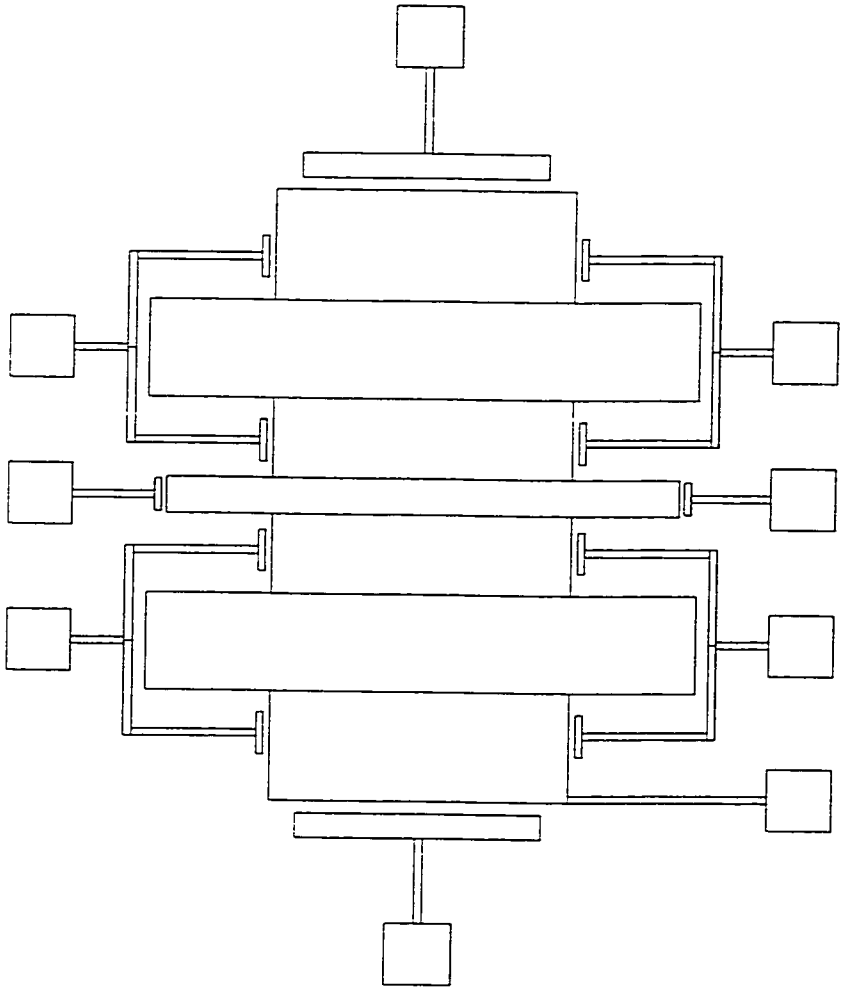

FIGURE B.1 Mask number 901

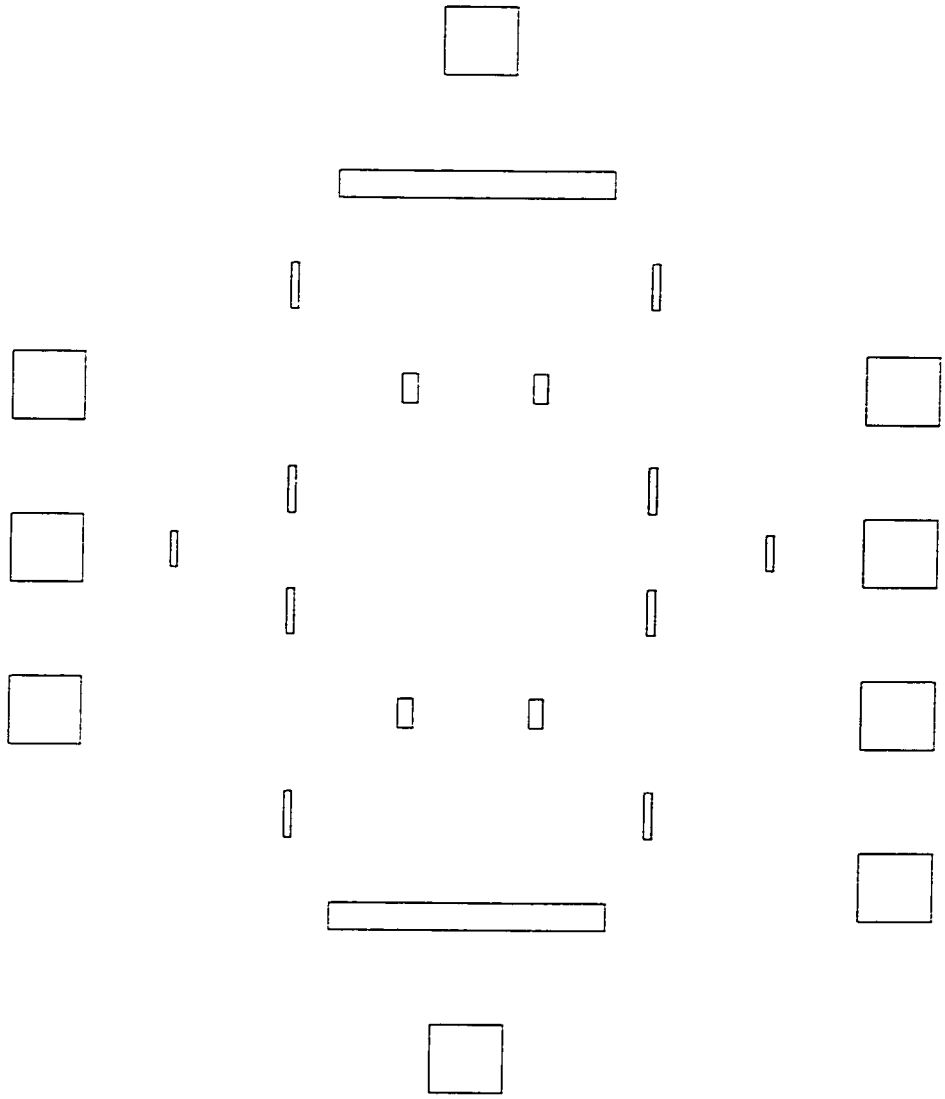

FIGURE B.2 Mask number 902

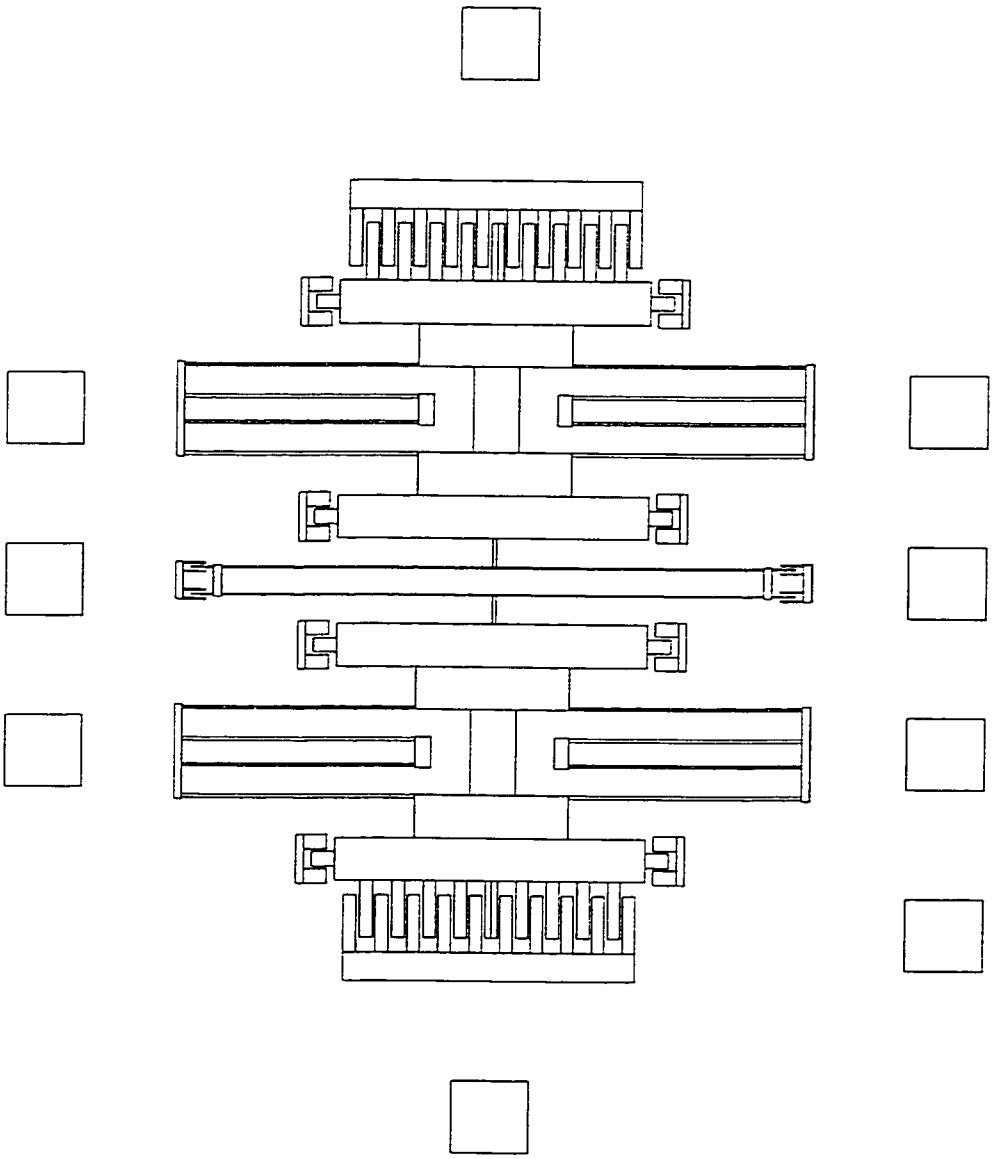

FIGURE B.3 Mask number 903

References

1. L. L. Roger, T. Howe, and A. P. Pisano, "Microelectromechanical Filters for Signal Processing", IEEE J. Microelectromech. Syst., vol. 7, pp. 286-294, 1997.

2. W. C. Tang, T. C. Nguyen, and R. T Howe, "Laterally driven polysilicon resonant microstructures", Sens. Actuators, vol. 20, pp. 25-32, 1989.

3. W. C. Tang, T. C. Nguyen, and M. W. Judy, "Electrostatic-comb drive of lateral polysilicon resonators", Sens. Actuators A-Physical, vol. 21, pp. 328-331, 1991.

4. R. A. Johnson, Mechanical Filters in Electronics. New York: Wiley, 1983.

5. H. Nathanson, W. E. Newell, R. A. Wickstrom, and J. R. Davis Jr., "The resonant gate transistor", IEEE Trans. Electron Devices, vol. ED-14, pp. 117-133, Mar. 1967

6. K. Wang, C. T. –C. Nguyen, "High-Order Medium Frequency Micromechanical Electronic Filters", IEEE J. Microelectromech. Syst., vol. 8, pp. 534-557, 1998.

7. R. Adler, "Compact electromechanical filters", Electronics, vol. 20, pp.100-105, 1947.

8. J. C. Hathaway and D. F. Babcock, "Survey of mechanical filters and their applications", Proc. IRE, vol. 45, pp. 5-16, Jan. 1957.

9. R. A. Johnson, M. Borner, and M. Konno, "Mechanical filters – A review of progress", IEEE Trans. Sonics Ultranson., vol. SU – 18, pp. 155-170, 1971.

10. Y. H. Cho, B. M. Kwak, A. P. Pisano, and R. T. Howe, "Viscous energy dissipation in laterally oscillating planar microstructures: A theoretical and experimental study", in Proc. IEEE Micro Electro Mechanical Systems Workshop (MEM93), PP. 93-98, 1993.

11. L. Lin, C. T.-C. Nguyen, R. T. Howe, and A. P. Pisano, Microelectromechanical Signal Processors, U.S. Patent 5 455 547, 1995.

12. X. Zhang and W. C. Tang, "Viscous air damping in laterally driven microresonators", in IEEE Micro Electro Mechanical Systems Workshop MEMS94, pp. 199-204, 1994.

13. C. T.-C. Nguyen and R. T. Howe, "Microresonator frequency control and stabilization using an integrated micro oven", in Dig. Transducers'93, Int. Conf. Solid-State Sensors and Actuators, pp. 1040-1043, 1993.

14. C. T.-C Nguyen, "Micromechanical signal processors", Ph.D. dissertation, Dept. Elec. Eng. Comput. Sci., Univ. California-Berkeley, Dec. 1994.

15. K. Wang, and C. T.-C. Nguyen, "High-Order Medium Frequency Micromechanical Electronic Filters", IEEE J. Microelectromech. Syst., vol. 8, pp. 534-557, 1999.

16. W. A. Johnson, and L. K. Warne, "Electrophysics of Micromechanical Comb Actuators", IEEE J. Microelectromech. Syst., vol. 4, pp. 49-59, 1995.

17. A.-C. Wong, J. R. Clark, and C. T.-C. Nguyen, "Anneal-Activated, Tunable, 68MHz Micromechanical Filters", Digest of Technical Papers, 10th International Conference on Solid-State Sensors and Actuators, Sendai, Japan, June7-10, 1999, pp. 1390-1393.

18. C. T.-C. Nguyen, Ark-Chew Wong, Hao Ding, "Tunable, Switchable, High-Q VHF Micromechanical Bandpass Filters", IEEE International Solid-State Circuits Conference, 1999.

19. L. Lin, C. T.-C. Nguyen, R. T. Howe, and A. P. Pisano, Microelectromechanical Signal Processor Fabrication, U.S. Patent 5 589 082, Dec. 1996.

20. J. T. Taylor, Q. Huang, R. A. Johnson, "CRC Handbook of Electrical Filters", ISBN 0-8493-8951-8, CRC Press LLC, 1997.

21. R. Frisch-Fay, "Flexible Bars", UDC number 539.384: 62-127, Butterworth & Co. Ltd, 1962.

22. W. C. Tang, M. G. Lim, and R. T. Howe, "Electrostatic Comb Drive Levitation and Control Method", IEEE J. Microelectromech. Syst., vol. 1, pp. 170-178, 1992.

23. T. Hirano, T. Furuhata, K. J. Gabriel, and H. Fujita, "Design, Fabrication and Operation of Submicron Gap Com-Drive Microactuators", IEEE J. Microelectromech. Syst., vol. 1, pp. 52-59, 1992.

24. W. C. Tang, R. T. Howe, Laterally Driven Resonant Microstructures, U.S. Patent 5 025 346, Jun. 1991.

25. S. O. Oyadiji, "Controlling the Vibrations of Beams Using Viscoelastic Potting", University of Manchester, UK.

26. N. S. Nise, "Control Systems Engineering", ISBN 0-8053-5424-7, Addison-Wesley Publishing Company, Second Ed., 1995.

27. Kun Wang, Clark T. –C. Nguyen, "High-Order Micromechanical Electronic Filters", IEEE J., 1997.

28. Philip Gillett, "Calculus and Analytical Geometry", ISBN 0-669-00641-6, D. C. Heath and Company, 1981.

29. James Stewart, "Calculus Early Transcendentals", ISBN 0-534-25158-7, Brooks/Cole Publishing Company, 1995.

30. IntelliSuite Training Manual, version 4.0 May 1999.

31. IntelliSuite User's Manual, version 4.0 May 1999.

32. James B. Dabney, Thomas L. Harman, "Mastering Simulink 2", ISBN 0-13-243767-8, Prentice-Hall, Inc. 1998.

33. Daniel Keating at IntelliSuite

34. S. Diamantis, M. Ahmadi, G. A. Jullien and W. C. Miller, "A Programmable MEMS Bandpass Filter", IEEE Mid-West Symposium on Circuits and Systems, August 2000, *(in Press).*

VITA AUCTORIS

Sotirios Diamantis was born in 1977 in Windsor, Ontario. He graduated from E. J. Lajeuness High School in 1995. From there he went on to the University of Windsor where he obtained a B.A.Sc. in Electrical Engineering in 1999. He is currently a candidate for the Master's degree in Electrical Engineering at the University of Windsor and will graduate in the fall 2000 convocation.